Simulation of polymer melts using Radial Basis Function and Brownian configuration field method

Hung Quoc Nguyen[1], Canh-Dung Tran[1*]

[1]School of Engineering, University of Southern Queensland, West Street, Darling Heights, Toowoomba, Queensland QLD 4350, Australia.

[*]Corresponding author: canh-dung.tran@unisq.edu.au

Abstract: Polymer melts are viscoelastic fluids and extremely complex fluids due to the existence of very high density of polymer molecules. Polymer melt rheology aims to understand and quantify the viscous and elastic properties of a polymer. In this work, the Integrated Radial Basis Function based Brownian configuration fields (IRBF - BCF) is further developed to simulate the dynamic behaviours of polymer melt flows. For the method, a polymer melt is governed by the macro-micro governing equations, which is processed for the solution of the primitive variables (velocity and pressure fields, and the kinetic behaviours of polymer melt for the flow's stress tensor). In this paper, polymer melt is modelled using "single-segment" reptation models or tube models where the polymer stress is averagely computed from an ensemble of thousands of tube segments at each grid point. The use of a Cartesian grid-based 1D-Integrated RBF (IRBF) approximation not only helps to avoid any complex meshing process but also to ensure a fast convergence rate for the solution of macro-micro governing equations. Furthermore, the use of BCF maintains the correlation of polymer stress fields in the simulation and hence enhances the numerical stability of the method. As an illustration of the method, the start-up Couette polymer melt flow and the polymer melt flow over a cylinder in a channel are investigated using four classical reptation models including the Doi-Edwards, Curtiss-Bird, Reptating Rope and Double Reptation models.

Keyword: Brownian configuration fields, Integrated Radial Basis Function, polymer melt, Doi and Edwards model, reptation models.

1. Introduction

Polymer melts and concentrated polymer solutions are extremely complex fluids due to the existence of very high density of polymer molecules. The behaviours of solutions or molten polymers have become increasingly relevant to their engineering processing techniques, requiring the development of efficient simulation methods. In polymer melts, the motion of a molecule is very difficult because of the movement restraint by other ones. Thus, a polymer chain only can move along its backbone and the motion in the perpendicular direction to the backbone is mostly limited by surrounding polymers [1] . Therefore, the motion of a molecule in an undiluted polymer system is assigned to a so-called reptational motion [2]. In a publication on the use of reptation theory to model undiluted polymer systems, Doi and Edwards assumed each polymer chain in a highly concentrated system reptates in a fictitious tube created by its neighbouring molecules [3]–[5] . Based on the reptation concept, Curtiss and Bird (CB) model uses an anisotropic friction tensor instead of using the "tube" constraint to describe the limit of the sideways motion of polymers in the DE model [6]–[9]. Furthermore, other reptation based models for the simulation of undiluted polymers such as Reptating Rope (RR) and Double Reptation (DR) models were developed. While the former one considers the interaction between segments in each polymer chain [10], [11], the latter one takes into account of the effect of the constraint release mechanism [12]. Recently, Ottinger developed the theory of stochastic processes which relates to kinetic theoretical models governed by a corresponding diffusion equation [13][14]. In this approach, the diffusion equation is transformed into the stochastic differential equation whose physical meaning is completely maintained while the numerical simulation method for kinetic models is very elegant.

Over the last two decades, the stochastic macro-micro methods have been contributing significantly into the simulation of viscoelastic flows including dilute polymer solutions, liquid crystals and polymer melts. Basically, the "macro-micro" term based on the fact that the governing conservation equations in continuum mechanics are coupled with the coarse-grained molecular models of kinetic theory for the solution of viscoelastic flow problems. Ottinger and co-workers proposed the 'Calculation of Non-Newtonian Flow: Finite Elements and Stochastic Simulation Technique' (CONNFFESSIT) method [15]. One of the noticeable characteristics of the CONNFFESSIT is that the polymer stress field is calculated from the configuration distribution of coarse-grained molecules (dumbbells) instead of using a constitutive equation. Due to this great advantage, the method has become a preferable choice for rheologists in finding out the dynamics characteristics of polymer flows without the need of a closed form constitutive equation [16]. The Eulerian approach of this method named Brownian configuration field (BCF) [17] uses an ensemble of continuous configuration fields which are convected and deformed by the drift components including the velocity gradient of the flows, elastic forces and the Brownian diffusion motion in the simulation. In an alternative approach, Tran-Canh and Tran-Cong developed an RBF-based

stochastic macro-micro mesh-free method using both Lagrangian and Eulerian approaches to simulate dilute polymer solutions [18], [19]. Follow the approach, the domain under consideration is discretised by a set of uniform or random collocation points instead of using an element-based method. Thus, it is more flexible than the CONNFFESSIT for the solution of problems with complex geometries, moving boundary and free surface. High performance computing with domain decomposition and parallel computation was also applied efficiently in the method to deal with the large-scale feature of problems [20] . The method has been further developed with the use of the integrated RBF (IRBF) [21], [22] in discretising partial differential governing equations of the system to enhance the convergence rate as well as reduce the white noise of the multiscale method [23]–[25] . In this paper, the IRBF-BCF-based coarse-grained method [25]–[27] is further developed and extended to simulate polymer melt systems using reptation models in transient flows.

The paper is organized as follows. The conservation equations of mass and momentum for a polymer melt flow are presented in Section 2. Section 3 is a review of several key "single-segment" reptation models used in the simulation. Also, the micro governing equations and the extra stress formula for each model are presented. A general system of macro-micro governing equations is presented in section 4. The present IRBF − BCF based stochastic multiscale method for the simulation of polymer melts is detailed in section 5 together with several noticeable points of the present algorithm. The numerical examples of the start-up Couette flow and the benchmark flow past a cylinder are illustrated in section 6. Finally, the paper is closed by a conclusion in section 7.

2. Governing equations of a polymer melt flow

The flow of an incompressible and isothermal polymer melt is governed by the following conservation equations of mass and momentum

$$\nabla \cdot \mathbf{u} = 0, \tag{1}$$

$$\rho \frac{D\mathbf{u}}{Dt} = -\nabla p + \nabla \cdot \boldsymbol{\tau}_p, \tag{2}$$

Where $\frac{D}{Dt}(\bullet)$ is the material derivative and defined by $\frac{D}{Dt}(\bullet) = \frac{\partial}{\partial t}(\bullet) + \mathbf{u} \cdot \nabla(\bullet)$, $\mathbf{u}$ the velocity field; p the hydrostatic pressure; ρ the polymer melt density; $\boldsymbol{\tau}_p$ the polymer stress tensor. It is worth noting that since the melt density is very high, the motion of polymer molecules is strictly constrained from other ones. Thus, the behaviour of polymer melt flow are mostly dominated by the viscous component rather than inertia one and the motion equation of polymer melt flows is rewritten as

$$-\nabla p + \nabla \cdot \boldsymbol{\tau}_p = 0 \tag{3}$$

Polymer melts behave like an inertialess flow without any contribution from solvent viscosity. However, its numerical solution is very difficult to be obtained because the macro velocity field becomes oscillating in the absence of the solvent viscosity. This instability in simulations of molten polymer system was mentioned by [28] [29] . In their papers, a "numerical damping term" was added into the inertialess momentum equation to make sure that a large change between two iterations cannot occur. So, the momentum equation for molten polymer flow is now modified as [29]

$$-\nabla p + D_P \nabla^2 \left(\mathbf{u} - \mathbf{u}_0 \right) + \nabla \cdot \boldsymbol{\tau}_P = 0, \tag{4}$$

where D_P is the numerical damping parameter in a polymer melt simulation; p, $\boldsymbol{\tau}_p$ and $\mathbf{u}_0$ the known pressure, polymer stress and velocity fields, respectively, of the previous time step and $\mathbf{u}$ the unknown current velocity field. It should be noted that when the velocity field achieves the stable state, that is $\mathbf{u} \approx \mathbf{u}_o$, the "damping term" disappears and Eq. (4) returns its original inertialess momentum equation for polymer melt Eq. (3).

In the macroscopic approach the system (1) and (4) is usually closed by a constitutive equation using several models of polymer melts such as K-BKZ [30] [31]), PTT model [32] or Pom-Pom models [33] for the polymer-contributed stress $\boldsymbol{\tau}_p$. In contrast, $\boldsymbol{\tau}_p$ is here numerically determined via a coarse-grained technique [1], [34] using reptation models. An overall microscopic procedure is described in the next section.

3. Review on stochastic macro-micro method for polymer melt flows using reptation models

For this approach, the determination of polymer stress tensor is performed through two steps: (i) the first step is to derive the diffusion equation or Fokker-Planck equation for the configurational distribution function, which is the probability density of the polymer configuration, presented by the unit vector (**P**), occurring at time (*t*); and (ii) the second step is to develop an expression for the stress tensor corresponding to reptation models [34]. The stochastic simulation is based on the relationship between the diffusion equation and the stochastic differential equation (SDE). In polymer kinetic theory, polymer melts and concentrated polymer solutions are often represented in the form of tube or reptation models [35]. For the reptation concept, the evolution of tube configurations is determined and the polymer melt stress tensor is updated at each and every time step based on the obtained configurations of the tube model. In this paper, "single-segment" tube models including the DE, CB, RR and DR models are considered using BCF based stochastic simulation technique.

For this approach, two characteristics of the segment monitored by the unit vector **P** along the segment and the position of the segment on the tube S, with S $\in$[0, 1] where S = 0 and S = 1 are two ends of the tube. It is worth noting that, the two characteristic quantities **P** and S of the stochastic process are

governed by two separate differential equations. The stochastic and deterministic differential equations and the polymer stress formula of reptation models are briefly presented in the next sub-sections.

3.1. Doi-Edwards and Curtiss-Bird models

The DE and CB models are based on the diffusion equation for a probability density function ψ (**p**, s, t) as follows (Doi and Edwards, 1978a)

$$\frac{\partial \psi(\mathbf{p},s,t)}{\partial t} = -\frac{\partial}{\partial \mathbf{u}} \cdot \left\{ \left[(\nabla \mathbf{u}(t))^T \cdot \mathbf{p} - (\nabla \mathbf{u}(t))^T : \mathbf{ppp} \right] \psi(\mathbf{p},s,t) \right\} + \frac{1}{\lambda} \frac{\partial^2 \psi(\mathbf{p},s,t)}{\partial s^2}, \qquad (5)$$

where **p** is a 3-D unit vector describing the direction of polymer at the position s (s $\in$ [0,1]); $(\nabla \mathbf{u})^T$ the transposed velocity gradient tensor and λ a characteristic or reptation time constant. The boundary condition for s = 0 and s = 1 is $\psi(\mathbf{p},0,t) = \psi(\mathbf{p},1,t) = \delta(|\mathbf{p}|-1)/4\pi$ where δ is the Dirac delta function.

The system of deterministic and stochastic differential equations of a stochastic process (**P**, S) corresponding to the DE and CB models derived from Eq. (5) is given by ([29])

$$d\mathbf{P}(\mathbf{x},t) = (\mathbf{I} - \mathbf{PP}) \cdot (\nabla \mathbf{u}(\mathbf{x},t))^T \cdot \mathbf{P}(\mathbf{x},t) dt - \mathbf{u}(\mathbf{x},t) \cdot \nabla \mathbf{P}(\mathbf{x},t) dt, \qquad (6a)$$

$$dS = \sqrt{\frac{2}{\lambda}} dW(t), \qquad (6b)$$

where $\mathbf{I}$ is the identity matrix or tensor; W(t) the 1-D time-dependent Wiener process; and **P** and S (S $\in$ [0,1]) are the unit vector and real value associated with **p** and s, respectively. Since two characteristics **P** and S of the stochastic process are governed by two separate differential equations (6a) and (6b), respectively, when S goes beyond the limits (S < 0 or S > 1). A refection needs to be done as follows: S $\rightarrow$ -S for S < 0, and S $\rightarrow$ (2 − S) for S > 1. In such cases, the configuration field **P**'s is randomly re-initialized.

The polymer stress tensor associated with the DE and CB models is given by

$$\boldsymbol{\tau}_p(t) = N n_p k_B T \left[\frac{1}{3} \mathbf{I} - \langle \mathbf{PP} \rangle - l_1 \lambda (\nabla \mathbf{u})^T : \langle S(1-S)\mathbf{PPPP} \rangle \right] \qquad (7)$$

where T is the absolute temperature; k_B the Boltzmann constant; n_p the density of polymers; N the number of beads of a Kramers chain; $\langle \mathbf{PP} \rangle$ the statistical average of **PP**; and l_1 ($l_1 \in [0,1]$) the link tension coefficient [6],[7]. The stress tensor presented in Eq. (7) is for the DE model with $l_1 = 0$.

3.2. Reptating Rope model

In the RR model, each polymer molecule is considered as an elastic rope moving in a constraining tube and the interaction between segments within a single chain plays an important role in the simulation of

polymer melt flows. Thus, two reptation processes (**P**, S) and (**P'**, S') governed by Eqs. (6a)-(6b) are simultaneously processed to simulate flows of molten polymer [14] . The stress tensor of the model is determined as follows.

$$\boldsymbol{\tau}_p(t) = N n_p k_B T \left[\frac{1}{3}\mathbf{I} - \langle \mathbf{PP} \rangle \right] + \Delta\boldsymbol{\tau}_p, \tag{8}$$

where $\Delta\boldsymbol{\tau}_p$ (t) is given by

$$\Delta\boldsymbol{\tau}_p = -\frac{1}{2} n_p k_B T \lambda (\nabla\mathbf{u})^T : \left\langle \left(S + S' - \left| S - S' \right| - 2SS' \right) \mathbf{P'P'PP} \right\rangle. \tag{9}$$

It is be noted that S and S′ are two separate segments within the same polymer chain; **P** and **P'** denote the direction of the two segments S and S', respectively.

To consider the correlation between the two reptation processes, a length parameter δ ($0 \le \delta \le 1$) is introduced into the simulation [34] . If the difference |S - S'| is larger than δ, the processes have no correlation and the directions of **P** and **P'** are independent with each other. Otherwise, their directions are coincident.

3.3. Double Reptation model

In the DR model, a constraint release mechanism is introduced into the evolution of **P**. The system of deterministic and stochastic differential equations is now given by [34].

$$d\mathbf{P}(\mathbf{x},t) = (\mathbf{I}-\mathbf{PP}) \cdot \left[(\nabla\mathbf{u})^T \cdot \mathbf{P}dt + \frac{\pi l_2}{\sqrt{3\lambda}} d\mathbf{W}_2(t) \right] - \frac{\pi^2 l_2^2}{\sqrt{3\lambda}}\mathbf{P}dt - \mathbf{u}\cdot\nabla\mathbf{P}dt, \tag{10a}$$

$$dS = \sqrt{\frac{2}{\lambda}}d\mathbf{W}_1(t), \tag{10b}$$

where l_2 is the real number related to the reptation coefficient l'; **W**$_2$ the 3-D Wiener process describing the effect of constraint release which was introduced into the DE and CB models. The corresponding stress tensor for the DR model is determined as follows.

$$\boldsymbol{\tau}_p(t) = N n_p k_B T \left[\frac{1}{3}\mathbf{I} - \langle \mathbf{PP} \rangle - l_1 \lambda (\nabla\mathbf{u})^T : \langle S(1-S)\mathbf{PPPP} \rangle - l_3 \lambda (\nabla\mathbf{u})^T : \langle \mathbf{PPPP} \rangle \right], \tag{11}$$

where l_3 is the dimensionless parameter defined from experimental or theoretical methods; and others defined above. It is worth emphasising that the system Eq. 10.a&b can be considered as the general form for classical reptation models.

4. A coupled macro-micro multiscale system for molten polymer flows using the reptation models

Collecting the differential conservation equations Eq. (1) & (4), the BCF stochastic differential equations of tube segments, the Brownian motion of the random walker and the stress tensor using the classical reptation models yields a macro-microscopic multiscale system as follows,

$$\nabla \cdot \mathbf{u} = 0, \tag{12a}$$

$$D_p \nabla^2 \left(\mathbf{u} - \mathbf{u}_0 \right) + \nabla \cdot \boldsymbol{\tau}_p - \nabla p = 0, \tag{12b}$$

$$d\mathbf{P}(\mathbf{x},t) = (\mathbf{I} - \mathbf{PP}) \cdot \left[(\nabla \mathbf{u})^T \cdot \mathbf{P} dt + \frac{\pi l_2}{\sqrt{3\lambda}} d\mathbf{W}_2(t) \right] - \frac{\pi^2 l_2^2}{\sqrt{3\lambda}} \mathbf{P} dt - \mathbf{u} \cdot \nabla \mathbf{P} dt, \tag{12c}$$

$$dS = \sqrt{\frac{2}{\lambda}} d\mathbf{W}_1(t), \tag{12d}$$

$$\boldsymbol{\tau}_p = N n_p k_B T \left[\frac{1}{3} \mathbf{I} - \langle \mathbf{PP} \rangle - l_1 \lambda (\nabla \mathbf{u})^T : \langle S(1-S) \mathbf{PPPP} \rangle - l_3 \lambda (\nabla \mathbf{u})^T : \langle \mathbf{PPPP} \rangle \right] + l_4 \Delta \boldsymbol{\tau}_p, \tag{12e}$$

All parameters in Eqs. (12)a, b, c, d and e were defined in previous sections. It is worth noting that the system of macro-micro equations (12) is generally developed for all reptation models. Specifically, with $l_1 = l_2 = l_3 = l_4 = 0$ the equations are for the DE model; $l_2 = l_3 = l_4 = 0$ for the CB model; $l_1 = l_2 = l_3 = 0$ for the RR model; and $l_4 = 0$ for the DR model.

Let U_c and L_c be the characteristic velocity and length, respectively; $t_c = L_c/U_c$ the macroscopic characteristic time; $\tau_p = \lambda/\pi^2$ the characteristic relaxation time of reptation models used in this work. Dimensionless variables corresponding to pressure (p), stress tensor ($\boldsymbol{\tau}_p$), velocity (**u**) and time (t) are given by [29]

$$p^* = p \frac{L_c}{\eta_0 U_c}, \qquad \boldsymbol{\tau}_p^* = \boldsymbol{\tau}_p \frac{L_c}{\eta_0 U_c}, \qquad \mathbf{u}^* = \frac{\mathbf{u}}{U_c}, \qquad t^* = \frac{t}{t_c} \tag{13}$$

where η_0 is the zero-shear-rate viscosity. Other parameters were defined before. The dimensionless Weissenberg number *We* is defined as $We = \dfrac{\tau_d}{t_c} = \dfrac{\lambda U_c}{\pi^2 L_c}$.

The stochastic multiscale system Eqs. (12a) - (12e) are rewritten in dimensionless form as

$$\nabla^* \cdot \mathbf{u}^* = 0, \tag{14a}$$

$$D_P^* (\nabla^*)^2 \left(\mathbf{u}^* - \mathbf{u}_0^* \right) + \nabla^* \cdot \boldsymbol{\tau}_p^* - \nabla^* p^* = 0, \tag{14b}$$

$$d\mathbf{P}(\mathbf{x},t) = (\mathbf{I} - \mathbf{PP}) \cdot \left[(\nabla^* \mathbf{u}^*)^T \cdot \mathbf{P} dt^* + \frac{\pi l_2}{\sqrt{3We}} d\mathbf{W}_2^* \right] - \frac{\pi^2 l_2^2}{3We} \mathbf{P} dt^* - \mathbf{u}^* \cdot \nabla^* \mathbf{P} dt^*, \tag{14c}$$

$$dS = \sqrt{\frac{2}{\pi^2 We}} dW_1^*,$$

(14d)

$$\boldsymbol{\tau}_p^* = \left[Nn_p k_B T \right]^* \left[\frac{1}{3}\mathbf{I} - \langle \mathbf{PP} \rangle - l_1 \pi^2 We \left(\nabla^* \mathbf{u}^* \right)^T : \langle S(1\text{-}S)\mathbf{PPPP} \rangle - l_3 \pi^2 We \left(\nabla^* \mathbf{u}^* \right)^T : \langle \mathbf{PPPP} \rangle \right] + l_4 \Delta \boldsymbol{\tau}_p^*,$$

(14e)

Where $\Delta \boldsymbol{\tau}_p^*$ is given by

$$\Delta \boldsymbol{\tau}_p^* = -\frac{1}{2} \left[n_p k_B T \right]^* \pi^2 We \left(\nabla^* \mathbf{u}^* \right)^T : \left\langle \left(S + S' - \left| S - S' \right| - 2SS' \right) \mathbf{P'P'PP} \right\rangle.$$

(15)

In Eqs. (14) - (15), the asterisk symbol (*) indicates the dimensionless form of variables. It should be pointed out that $[Nn_p k_B T]^*$ and $[n_p k_B T]^*$ depict the dimensionless form of $Nn_p k_B T$ and $n_p k_B T$ (stress dimension), respectively. Henceforth, all variables will be written in the dimensionless form and the asterisk symbol will be removed for simplicity.

5. Present numerical method for polymer melts using reptation models

In this section, the spatial and temporal discretisations for the hybrid system of macro-micro governing equations are presented in detail. In the macro procedure, the 1D-IRBF scheme is applied to spatially discretise the conservation equations (14a) & (14b). For the micro procedure, the stochastic differential equations (14c) & (14d) are advanced with respect to time using a simple Euler explicit scheme coupled with IRBF scheme.

5.1. IRBF based projection method for solving the macroscopic governing equations

5.1.2. Review on 1D-IRBF based spatial discretisation scheme

At each time step, consider a second-order partial differential equation. On an x-gridline which consists of N_x collocation points, the 1D-IRBF scheme is used to construct the expressions for the second derivative, the first derivative and the original function u as follows ([27] [36]

$$\frac{\partial^2 \mathbf{u}(x)}{\partial x^2} = \sum_{i=1}^{N_x} w_i g_i(x) = \sum_{i=1}^{N_x} w_i G_i^{[2]}(x)$$

(16a)

$$\frac{\partial \mathbf{u}(x)}{\partial x} = \sum_{i=1}^{N_x} w_i G_i^{[1]}(x) + C_1$$

(16b)

$$u(x,t) = \sum_{i=1}^{N_x} w_i G_i^{[0]}(x) + C_1 x + C_2 \tag{16c}$$

where $\{w_i\}_{i=1}^{N_x}$ is the set of unknown RBF weights which need to be determined; $\{g_i(x)\}_{i=1}^{N_x}$ is the set of Multi-quadric RBFs (MQ-RBFs) which are directly calculated from the coordinates of collocation points; $G_i^{[1]}(x) = \int G_i^{[2]}(x) dx$, $G_i^{[0]}(x) = \int G_i^{[1]}(x) dx$ and C_1 and C_2 are the unknown constants of integration. The MQ-RBFs are given by

$$g_i(x) = \sqrt{(x - c_i)^2 - a_i^2} \tag{17}$$

Where $\{c_i\}_{i=1}^{N_x}$ and $\{a_i\}_{i=1}^{N_x}$ are the sets of centres and RBF widths, respectively. The centres coincide with the set of collocation point on the x-gridline.

A set of algebraic equations is obtained by applying equations (16a), (16b) and (16c) on all collocation points $\{x_i\}_{i=1}^{N_x}$,

$$\frac{\partial^2 \hat{\mathbf{u}}}{\partial x^2} = \hat{\mathbf{G}}^{[2]} \hat{\mathbf{w}}, \tag{18a}$$

$$\frac{\partial \hat{\mathbf{u}}}{\partial x} = \hat{\mathbf{G}}^{[1]} \hat{\mathbf{w}}, \tag{18b}$$

$$\hat{\mathbf{u}} = \hat{\mathbf{G}}^{[0]} \hat{\mathbf{w}}, \tag{18c}$$

where $\hat{\mathbf{w}} = \left(w_1, w_1, \ldots, w_{N_x}, C_1, C_2 \right)^T$ is a unknown vector consisting of the RBF weights and the two constants of integration; the other matrices and vectors are given by (Nguyen *et al.*, 2015)

$$\hat{\mathbf{u}} = \left(u(x_1), \quad u(x_2), \quad \cdots \quad u(x_{N_x}) \right)^T = \left(u_1, \quad u_2, \quad \cdots \quad u_{N_x} \right)^T \tag{19a}$$

$$\frac{\partial^k \hat{\mathbf{u}}}{\partial x^k} = \left(\frac{\partial^k u_1}{\partial x^k} \quad \frac{\partial^k u_2}{\partial x^k} \quad \cdots \quad \frac{\partial^k u_{N_x}}{\partial x^k} \right)^T \quad k = \{1,2\} \tag{19b}$$

$$\hat{\mathbf{G}}^{[2]} = \begin{bmatrix} G_1^{[2]}(x_1) & \cdots & G_{N_x}^{[2]}(x_1) & 0 & 0 \\ G_1^{[2]}(x_2) & \cdots & G_{N_x}^{[2]}(x_2) & 0 & 0 \\ \vdots & \ddots & \vdots & \vdots & \vdots \\ G_1^{[2]}(x_{N_x}) & \cdots & G_{N_x}^{[2]}(x_{N_x}) & 0 & 0 \end{bmatrix} \tag{19c}$$

$$\hat{\mathbf{G}}^{[1]} = \begin{bmatrix} G_1^{[1]}(x_1) & \cdots & G_{N_x}^{[1]}(x_1) & 1 & 0 \\ G_1^{[1]}(x_2) & \cdots & G_{N_x}^{[1]}(x_2) & 1 & 0 \\ \vdots & \ddots & \vdots & \vdots & \vdots \\ G_1^{[1]}(x_{N_x}) & \cdots & G_{N_x}^{[1]}(x_{N_x}) & 1 & 0 \end{bmatrix} \tag{19d}$$

$$\hat{\mathbf{G}}^{[0]} = \begin{bmatrix} G_1^{[0]}(x_1) & \cdots & G_{N_x}^{[0]}(x_1) & x_1 & 1 \\ G_1^{[0]}(x_2) & \cdots & G_{N_x}^{[0]}(x_2) & x_2 & 1 \\ \vdots & \ddots & \vdots & \vdots & \vdots \\ G_1^{[0]}(x_{N_x}) & \cdots & G_{N_x}^{[0]}(x_{N_x}) & x_{N_x} & 1 \end{bmatrix} \tag{19e}$$

The constants of integration are produced automatically from the IRBF-based approximation process. Thus, in order to get extra information from the system, one can easily incorporate additional constraints such as nodal derivative values into the algebraic equations as follows.

$$\begin{pmatrix} \hat{\mathbf{u}} \\ \hat{\mathbf{f}} \end{pmatrix} = \begin{bmatrix} \hat{\mathbf{G}}^{[0]} \\ \hat{\mathbf{L}} \end{bmatrix} \hat{\mathbf{w}} = \hat{\mathbf{C}}\hat{\mathbf{w}} \tag{20}$$

where $\hat{\mathbf{f}} = \hat{\mathbf{L}}\hat{\mathbf{w}}$ are the additional constraints. For the convenience, the network-weight space in the above equation should be converted into the physical space as follows

$$\hat{\mathbf{w}} = \hat{\mathbf{C}}^{-1} \begin{pmatrix} \hat{\mathbf{u}} \\ \hat{\mathbf{f}} \end{pmatrix} \tag{21}$$

where $\hat{\mathbf{C}}^{-1}$ is the conversion matrix. Based on the conversion in Eq. (21), the second and the first derivatives of u at each collocation point are rewritten as follows.

$$\frac{\partial^2 \mathrm{u}}{\partial x^2} = \mathbf{D}_{2x}\hat{\mathbf{u}} + k_{2x} \tag{22a}$$

$$\frac{\partial \mathrm{u}}{\partial x} = \mathbf{D}_{1x}\hat{\mathbf{u}} + k_{1x} \tag{22b}$$

where $\mathbf{D}_{1x}$ and $\mathbf{D}_{2x}$ are the known vectors of length N_x; and k_{1x} and k_{2x} are scalars determined by $\hat{\mathbf{f}}$. Applying Eqs. (22a) and (22b) on all collocation points on the x-grid-line yields

$$\frac{\partial^2 \hat{\mathbf{u}}}{\partial x^2} = \hat{\mathbf{D}}_{2x}\hat{\mathbf{u}} + \hat{\mathbf{k}}_{2x} \tag{23a}$$

$$\frac{\partial \hat{\mathbf{u}}}{\partial x} = \hat{\mathbf{D}}_{1x}\hat{\mathbf{u}} + \hat{\mathbf{k}}_{1x} \tag{23b}$$

Where $\hat{\mathbf{D}}_{1x}$ and $\hat{\mathbf{D}}_{2x}$ are the known matrices of dimension $N_x \times N_x$; $\hat{\mathbf{k}}_{1x}$ and $\hat{\mathbf{k}}_{2x}$ are the known vectors of length N_x.

A similar process is done for all collocation points on the y-gridline in order to obtain the values of the second and the first order derivatives of u. Details can be found in [23].

5.1.2. Temporal discretisation technique using the projection method for solution of primitive variables in macro procedure

The macroscopic governing equations (14a) - (14b) of a polymer melt is solved using the projection method and the algorithm includes 3 steps as follows

- Step 1: An intermediate velocity $\bar{\mathbf{u}}$ is calculated by solving Eq. (14b) with neglecting the pressure gradient term and incompressibility.

$$\frac{\bar{\mathbf{u}} - \mathbf{u}^n}{\Delta t} = D_p \nabla^2 \left(\bar{\mathbf{u}} - \mathbf{u}^n \right) + \nabla \cdot \boldsymbol{\tau}_p^n \qquad (24)$$

where Δt is the time step; $\mathbf{u}^n$ and $\boldsymbol{\tau}_p^n$ the known velocity vector and stress tensor, respectively, in the previous time step $t^n = n\Delta t$. The Dirichlet boundary conditions $\bar{\mathbf{u}} = \mathbf{u}^n$ are imposed on boundaries. Eq. (24) together with boundaries is solved using 1D-IRBF approximated scheme (see section 5.1.1)

- Step 2: Solve the Poisson equation for the pseudo pressure ϕ,

$$\nabla^2 \phi = \frac{1}{\Delta t} \nabla \cdot \bar{\mathbf{u}}, \qquad (25)$$

Where ϕ relates to the pressure p by the expression: $p = \phi - D_p \Delta t \left(\dfrac{\partial^2 \phi}{\partial x^2} + \dfrac{\partial^2 \phi}{\partial y^2} \right)$. The Neumann boundary condition for the solution of Eq. (25) is determined by

$$\mathbf{n} \cdot \nabla \phi = \frac{1}{\Delta t} \mathbf{n} \cdot \left(\bar{\mathbf{u}} - \mathbf{u}^n \right) \qquad (26)$$

Where $\mathbf{n}$ is the outward normal vector of the boundary. It is seen that the mass conservation equation (14a) is satisfied by the introduction of Eq. (25). The boundary value problem Eq. (25) is solved using 1D-IRBF scheme.

- Step 3: Determine the velocity field $\mathbf{u}^{n+1}$ at the current time step $t^{n+1} = (n+1)\, \Delta t$,

$$\mathbf{u}^{n+1} = \bar{\mathbf{u}} - \Delta t \nabla \phi \qquad (27)$$

5.2. BCF-based simulation technique for the evolution of polymer melt configurations

5.2.1. BCF algorithm for the simulation of a reptation process

In the present BCF-IRBFN multiscale approach, the analysis domain is discretised by a set of N collocation points instead of using a mesh of elements in the element based methods. At each collocation point, generate set of N_f tube segments $\mathbf{P}_i(\mathbf{x}, t)$ (i = 1, 2, 3, ..., N_f) attached to the point in the course of simulation. Therefore, there are N sets of N_f tube segments in total on the whole domain. $\mathbf{P}_i(\mathbf{x}, t)$ named as a configuration field is defined as a set of the tube segments having the same index i on the domain or, in other words, a configuration field consists of N tube segments indexed i on N collocation points. An illustrative example with N = 9 and N_f = 2 is presented in Fig. 1.
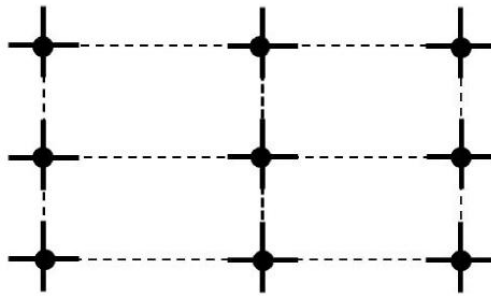

Figure 1. A typical example of configuration fields with N = 9 and N_f = 2. N: Number of collocation points; N_f: number of tube segments attached at each collocation point. Thus, there are two configuration fields: $\mathbf{P}_1(\mathbf{x}, t)$ and $\mathbf{P}_2(\mathbf{x}, t)$.

At the initial time, N_f configuration fields are uniformly initiated on all collocation points

$$\mathbf{P}_i(\mathbf{x}, 0) = \mathbf{P}_i^0 \qquad \left(i = 1, 2, 3, \ldots, N_f\right) \tag{28}$$

The initializing of a uniform tube configuration field yields an identical stress field on the whole domain, which reduces the numerical instability of the stress field in the simulation. The evolution of the configuration field is governed by the equation (14c) which is solved with the boundary condition of $S_i \in [0,1]$. However, since each tube segment makes a random walk S governed by Eq. (14d) through the reptation process, the initial correlation of the stress field is more likely to be degraded by the stochastic process. In order to fix this issue van Heel et al., (1999) proposed that each configuration field $\mathbf{P}_i(\mathbf{x}, t)$ associates with only one random walk S_i. When S_i is reflected at a boundary, a random unit vector is generated and assigned to all tube segments in the configuration field $\mathbf{P}_i(\mathbf{x}, t)$.

5.2.2 The Euler explicit method for temporal discretisation of the stochastic differential equations

The evolution of the polymer melt configuration in Eqs. (14c) and (14d) using the Euler explicit scheme is given for the characteristic **S** by

$$S_i^{n+1} = S_i^n + \sqrt{\frac{2\Delta t}{\pi^2 We}} W_{1i}^n, \tag{29}$$

where Δt is the time step; S_i^{n+1} and S_i^n values of S at two successive time steps $t^{n+1} = (n+1)\Delta t$ and $t^n = n\Delta t$, respectively; W_{1i} a single Gaussian random number and i presents the configuration field as described in the previous sub-section, and for the characteristic **P** by

$$\mathbf{P}_i^{n+1} = \mathbf{P}_i^n + \left(\mathbf{I} - \mathbf{P}_i^n \mathbf{P}_i^n\right)\left[\left(\nabla\mathbf{u}^n\right)^T \cdot \mathbf{P}_i^n \Delta t + \frac{l_2\sqrt{\Delta t}}{\sqrt{3We}}\mathbf{W}_i^n\right] - \frac{l_2^2}{3We}\mathbf{P}_i^n \Delta t - \mathbf{u}^n \cdot \nabla\mathbf{P}_i^n \Delta t, \tag{30}$$

where $\mathbf{u}^n$ and $\nabla\mathbf{u}^n$ are the velocity and velocity gradient at the time step n, respectively.

The Euler discretisation causes a significant error unless using sufficiently small time steps. Indeed, at time step t^n, if S^n is out of [0, 1], an observed reflection at boundaries is carried out. Otherwise, S^n could go beyond the limit [0, 1] during the time period ($t^n = n\Delta t$, $t^{n+1} = (n+1)\Delta t$). Thus, Ottinger (1989) proposed a treatment at boundaries S = 0 and S = 1 in the simulation of polymer melt flows using an unobserved reflection. The conditional probability to happen an unobserved reflection is given by

$$P_{ur} = e^{-\frac{\pi^2 We\left(b-S_i^n\right)\left(b-S_i^{n+1}\right)}{\Delta t}}, \tag{31}$$

where b is a boundary at which an unobserved reflection happens and determined as

$$\begin{bmatrix} b = 0 & \text{if } S_i^n + S_i^{n+1} \leq 1, \\ b = 1 & \text{if } S_i^n + S_i^{n+1} > 1. \end{bmatrix} \tag{32}$$

The unobserved reflection algorithm associated with the BCF approach for the treatment of stochastic process (**P**, S) is presented in Fig. 2.

5.3. Algorithm of the present method

The algorithm of the present Integrated RBF-BCF based macro-micro multiscale method for different reptation modelled polymer melts can be summarised as follows.

a) The simulation starts with N_f initial configurations of tube segments $\left(\mathbf{P}_i^0, i = 1, 2, \ldots, N_f\right)$ which are generated and uniformly distributed on every collocation point for the microscopic procedure. A set of N_f values of S_i in [0, 1] is also initiated corresponding with $\mathbf{P}_i^0$.

b) The stress tensor at every-point on the considered domain is calculated from a set of N_f tube segments assigned to each collocation point. A uniform polymer stress field is obtained at the first iteration because the initial molecular configurations are identical.

c) The projection method, presented in Sections 5.1, is applied to solve the conservation equations (14a) - (14b) for the new velocity and pressure fields.

d) The polymer configuration fields are processed by advancing the stochastic differential equations (14d) and (14c) of reptation models with respect to time using the improved algorithm presented in Fig. 2. The correlation of configurations is maintained at each time step because each configuration field associates with only one random walk S.
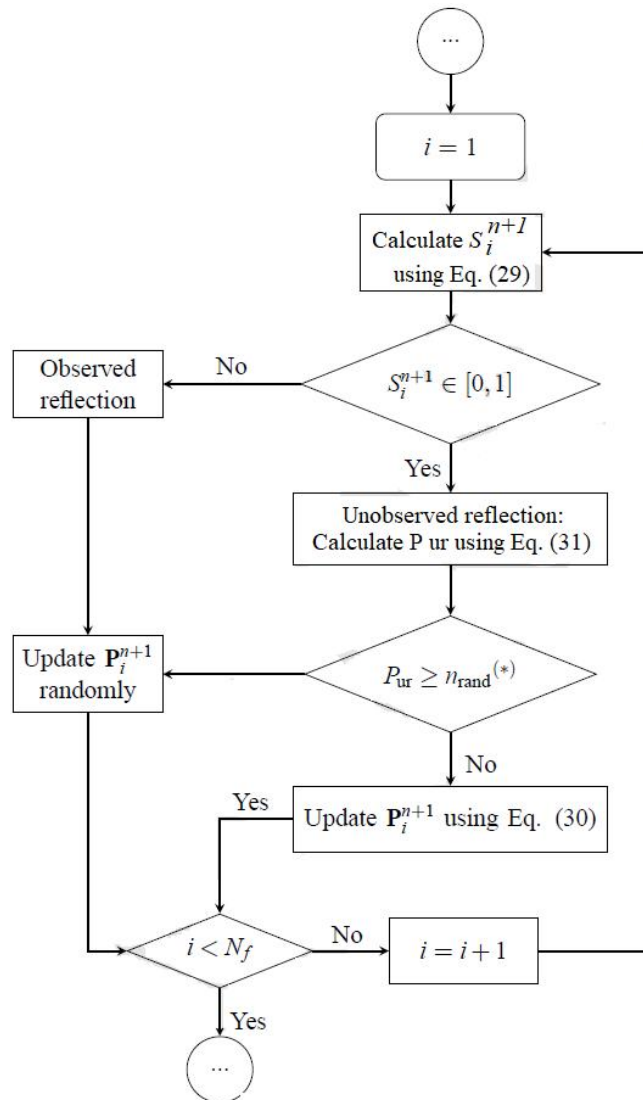

Figure 2. The BCF based unobserved reflection algorithm for the treatment of stochastic process (**P**, S). [*] n_{rand} is a single uniformly distributed random number in the interval (0, 1)

6. Numerical examples

In order to investigate and evaluate the present method for polymer melts, the start-up Couette flow and the flow past a cylinder in a long channel of polymer melts modelled by different reptation models are simulated. While results obtained by the simulation of the former problem are compared with those performed by [34], the solutions of the latter problem are verified with those by [29] for the DE model.

6.1 Start-up Couette flow of polymer melts with reptation models

The start-up Couette flow problem is presented in Fig. 3. It consists of two parallel plates, where the top plate is fixed while the bottom plate constantly moves with a velocity $U_c = 1$. The distance between two plates is scaled as $L_c = 1$.
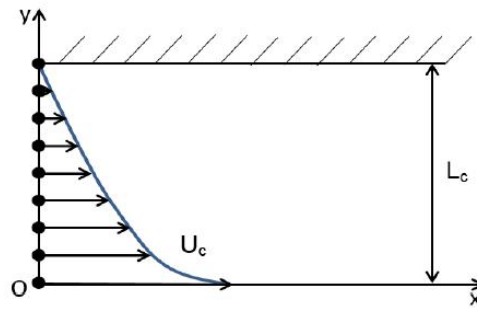

Figure 3. The start-up Couette flow problem. The collocation points and the velocity profile are schematically presented.

From the characteristic of the Couette flow problem of polymer melts, a system of stochastic macro-micro equations (12a, b, c, d, e) is developed as follows.

$$D_P\left(\frac{\partial^2 u}{\partial y^2}(y,t) - \frac{\partial^2 u_0}{\partial y^2}(y,t)\right) + \frac{\partial \tau_{p,xy}}{\partial y}(y,t) = 0 \tag{33}$$

$$dS(t) = \sqrt{\frac{2}{\pi^2 We}} dW_1(t), \tag{34}$$

$$\begin{cases} dP_x(y,t) = \frac{\partial u}{\partial y}(y,t)P_y(y,t)dt + \frac{l_2}{\sqrt{3We}}dW_{2x} - \frac{l_2^2}{3We}P_x(y,t)dt, \\[2mm] dP_y(t) = \frac{l_2}{\sqrt{3We}}dW_{2y} - \frac{l_2^2}{3We}P_y(y,t)dt, \\[2mm] dP_z(t) = \frac{l_2}{\sqrt{3We}}dW_{2z} - \frac{l_2^2}{3We}P_z(y,t)dt, \end{cases} \tag{35}$$

$$\begin{cases} \tau_{p,xx} = Nn_pk_BT\left[\frac{1}{3}-\langle P_xP_x\rangle -l_1\pi^2We\frac{\partial u}{\partial y}S(1\text{-}S)\langle P_xP_yP_xP_x\rangle -l_3\pi^2We\frac{\partial u}{\partial y}\langle P_xP_yP_xP_x\rangle\right]+\Delta\tau_{p,xx}, \\[3mm] \tau_{p,yy} = Nn_pk_BT\left[\frac{1}{3}-\langle P_yP_y\rangle -l_1\pi^2We\frac{\partial u}{\partial y}S(1\text{-}S)\langle P_xP_yP_yP_y\rangle -l_3\pi^2We\frac{\partial u}{\partial y}\langle P_xP_yP_yP_y\rangle\right]+\Delta\tau_{p,yy}, \\[3mm] \tau_{p,zz} = Nn_pk_BT\left[\frac{1}{3}-\langle P_zP_z\rangle -l_1\pi^2We\frac{\partial u}{\partial y}S(1\text{-}S)\langle P_xP_yP_zP_z\rangle -l_3\pi^2We\frac{\partial u}{\partial y}\langle P_xP_yP_zP_z\rangle\right]+\Delta\tau_{p,zz}, \\[3mm] \tau_{p,xy} = Nn_pk_BT\left[-\langle P_xP_y\rangle -l_1\pi^2We\frac{\partial u}{\partial y}S(1\text{-}S)\langle P_xP_yP_xP_y\rangle -l_3\pi^2We\frac{\partial u}{\partial y}\langle P_xP_yP_xP_y\rangle\right]+\Delta\tau_{p,xy}, \end{cases}$$

(36)

Where $\left(W_{2x},W_{2y},W_{2z}\right)$ and $\left(P_x,P_y,P_z\right)$ are 3 components of vectors $\mathbf{W_2}$ and $\mathbf{P}$, respectively; $\tau_{p,xx}$, $\tau_{p,yy}$, $\tau_{p,zz}$ and $\tau_{p,xy}$ the normal and shear stress components of $\boldsymbol{\tau}_p$. $\Delta\tau_{p,xx}$, $\Delta\tau_{p,yy}$, $\Delta\tau_{p,zz}$ and $\Delta\tau_{p,xy}$ are components of the stress contribution characterised by the RR model; and expressed by (see Eq. (15))

$$\begin{cases} \Delta\tau_{p,xx} = -\frac{1}{2}n_pk_BT\pi^2We\frac{\partial u}{\partial y}\left(S+S'-\left|S\text{-}S'\right|-2SS'\right)\langle P_x'P_y'P_x'P_x'\rangle, \\[3mm] \Delta\tau_{p,yy} = -\frac{1}{2}n_pk_BT\pi^2We\frac{\partial u}{\partial y}\left(S+S'-\left|S\text{-}S'\right|-2SS'\right)\langle P_x'P_y'P_y'P_y'\rangle, \\[3mm] \Delta\tau_{p,zz} = -\frac{1}{2}n_pk_BT\pi^2We\frac{\partial u}{\partial y}\left(S+S'-\left|S\text{-}S'\right|-2SS'\right)\langle P_x'P_y'P_z'P_z'\rangle, \\[3mm] \Delta\tau_{p,xy} = -\frac{1}{2}n_pk_BT\pi^2We\frac{\partial u}{\partial y}\left(S+S'-\left|S\text{-}S'\right|-2SS'\right)\langle P_x'P_y'P_x'P_y'\rangle, \end{cases}$$

(37)

where P_x', P_y' and P_z' are three components of the unit segment $\mathbf{P'}$; $\mathbf{S'}$ the position of $\mathbf{P'}$ in a rope model, and Δ the correlation length parameter related to the link tension coefficient l_1 and given by $\Delta = 1/(2l_1N)$ [34]

It is noted that while the Couette flow problem is a 1-D space, the micro configuration fields are processed in 3-D one. Hence, the time discretisation of the macro-microscopic governing equations (33), (34) and (35) using the numerical schemes presented in Section 5 yields

$$u^{n+1}-D_P\frac{d^2u^{n+1}}{dy^2}\Delta t = u^n - D_P\frac{d^2u^n}{dy^2}\Delta t+\frac{d\tau_{p,xy}^n}{dy}\Delta t$$

(38)

$$S^{n+1}=S^n+\sqrt{\frac{2\Delta t}{\pi^2We}}W_1^n,$$

(39)

$$
\begin{cases}
P_x^{n+1} &= P_x^n + \left(\dfrac{du}{dy}\right)^{n+1} P_y^n \Delta t + \dfrac{l_2 \sqrt{\Delta t}}{\sqrt{3We}} W_{2x}^n - \dfrac{l_2^2}{3We} P_x^n \Delta t, \\[3ex]
P_y^{n+1} &= P_y^n + \dfrac{l_2 \sqrt{\Delta t}}{\sqrt{3We}} W_{2y}^n - \dfrac{l_2^2}{3We} P_y^n \Delta t, \\[3ex]
P_z^{n+1} &= P_z^n + \dfrac{l_2 \sqrt{\Delta t}}{\sqrt{3We}} dW_{2z}^n - \dfrac{l_2^2}{3We} P_z^n \Delta t,
\end{cases}
\tag{40}
$$

where Δt is the time step size for both macro and micro procedures, the superscripts (n+1) and n depict the two successive time steps as t^{n+1} = (n+1) Δt and t^n = n Δt , respectively. The numerical damping parameter D_P is defined as $D_P = G \Delta t$, where $G = Nn_p k_B T$ is the rigidity modulus of the reptation model ([29]

6.1.1. Numerical results and discussion for the polymer melt flow using the DE model

For the simulation, polymer melt parameters include the fluid density ρ = 1, the zero-shear-rate viscosity $\eta_0^{DE} = 1$ and the relaxation time λ = 50 and Weiseenberg number of the polymer melt flow is defined as

$$
We = \frac{\lambda U_c}{\pi^2 L_c} = \frac{50}{\pi^2} \simeq 5.
$$

In this work, this problem, studied by [37] using the CONNFFESSIT approach, is simulated with the time step size $\Delta t = 0.001$ for both macro and micro procedures, the number of collocation points N_y = 21 and the number of configuration fields N_f = 2500 at each collocation point. Results by the present method shows a very good agreement with those by [37] using finer meshes (40 elements) and finer time step (Δt = 0.0001), evidenced by the following details.

- Fig. 4 depicts the evolution of the velocity profile in the considered domain: at the very early time (t = 0.25), the plate motion causes a perturbation on the velocity field at the region near the plate. Then, the momentum caused by the plate motion is successively transferred to next layers of polymer melt along the y-direction with a propagating speed c given by ([37]

$$
c^2 = \frac{12\eta_0^{DE}}{\rho\lambda},
\tag{41}
$$

where $\eta_0^{DE} = Nn_p k_B T \lambda / 60$ is the zero-shear-rate viscosity for the DE model and other parameters are defined as before. As a result, the polymer layer near the wall (see Fig. 3 - top plate) starts moving after t = 2 of the flow's start-up (see Fig. 4 at t = 2) using Eq. (41). The velocity then gradually decreases until reaching a stable state.

Fig. 4 also shows the existence of two separate shear regions at the stable state of a polymer melt Couette flow: (i) one area dominates most of the flow field ($y \in [0.1, 1]$) with very low velocity gradient and (ii) a narrow one near the moving plate ($y \in [0, 0.1]$) is influenced by a very high velocity gradient (see Fig. 5). This characteristic distinguishes polymer melt from dilute solutions in a shear flow as stated in [38][37][39][40].

- Due to the existence of two different shear rate zones in the flow, the velocity evolution at different locations are very distinct as shown in Fig. 6 where the evolution of velocity at locations y = 0.05, 0.1, 0.4 and 0.8 is presented. To be more specific, the velocity in the high shear-rate region at location y = 0.05 is significantly higher than ones in the low shear-rate zone at locations y = 0.1, 0.4 and 0.8. Furthermore, the overshoot of the velocity is always observed before reaching a stable value.
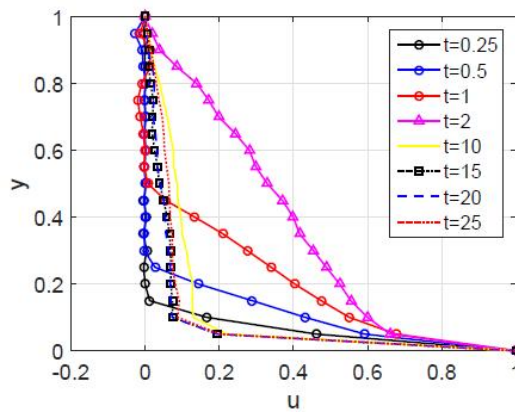

Figure 4. The start-up Couette flow simulation of polymer melt using the DE model: The evolution of velocity profile on whole domain.
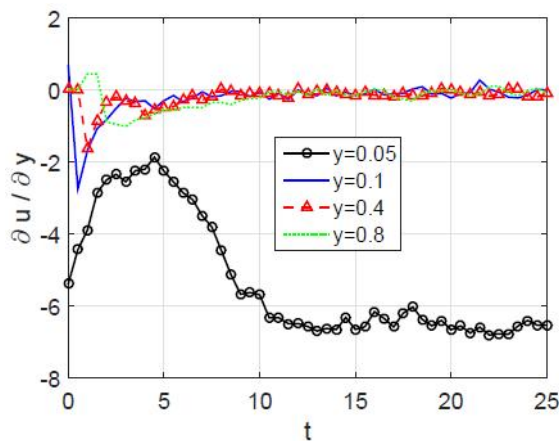

Figure 5. The start-up Couette flow simulation of polymer melt using the DE model: The velocity gradient with respect to time in the high shear-rate region at location *y* = 0.05 and the low shear-rate region at location *y* = 0.1, 0.4 and 0.8.
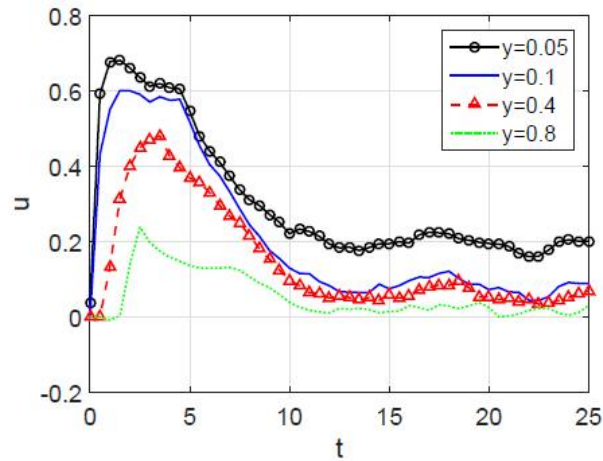
Figure 6. The start-up Couette flow simulation of polymer melt using the DE model: The evolution of velocity at locations y = 0.05, 0.1, 0.4 and 0.8
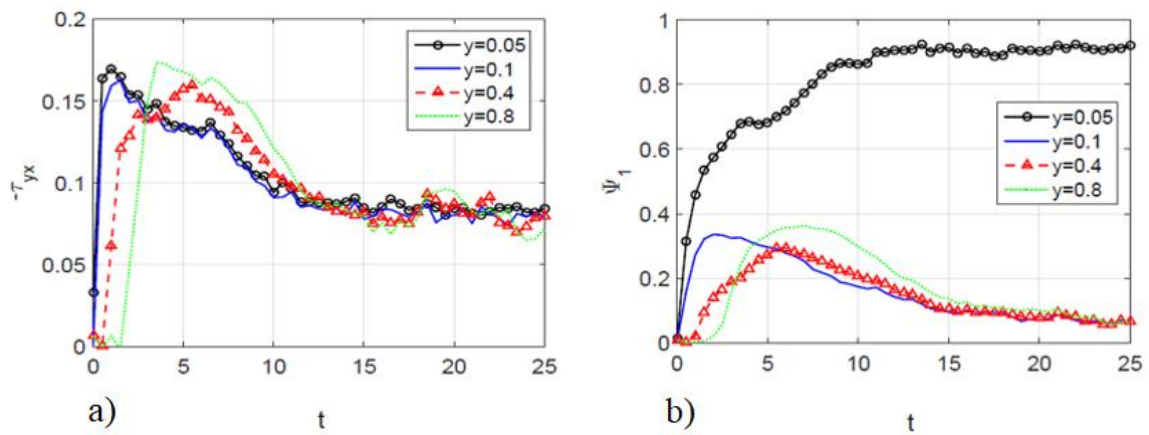

Figure 7. The start-up Couette flow simulation of polymer melt using the DE model: a) The evolution of the shear stress; and b) the first and second normal stress difference at in the high-shear-rate zone at location y = 0.05, 0.1, 0.4 and 0.8.

- The evolution of the shear stress and the first normal stress difference at locations y = 0.05, 0.1, 0.4 and 0.8 is shown in Figs. 7a & 7b, respectively. Results show that the shear stress is the nearly same at different positions (Fig. 7a) whereas the first normal stress difference is very distinct in the two shear rate areas (Fig. 7b). This typical behaviour of polymer melt in the start-up Couette flow was confirmed in [38]. Furthermore, the overshoot also appears in the evolution of shear stress at any location of the domain (Fig. 7a) whereas it only appears for the first normal stress difference in the low-shear-rate region (Fig. 7b). Results on the stresses' evolution in the high and low-shear-rate regions highlighted in Fig. 8 show that the second normal stress difference is always negative in both high and low-shear-rate regions, which agrees with experimental observations presented in [41] & [42].
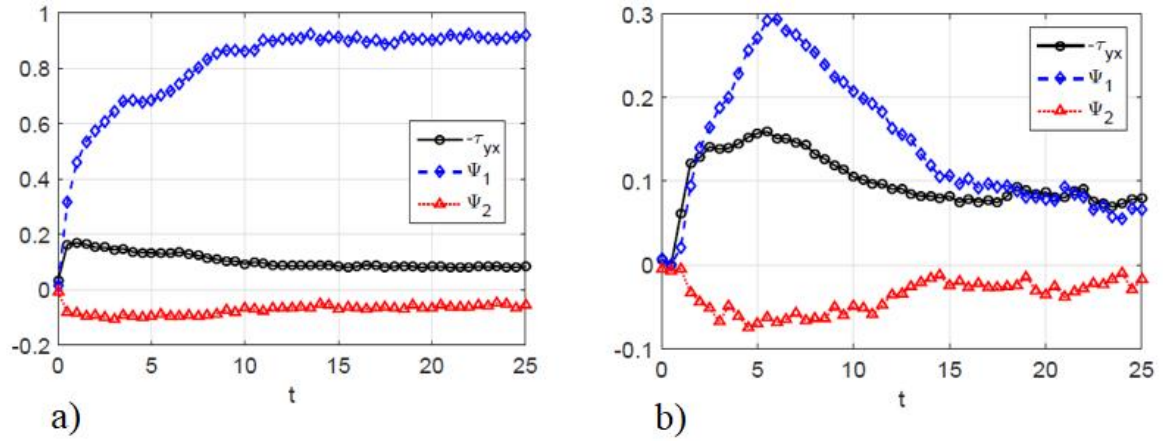
Figure 8. The start-up Couette flow simulation of polymer melt using the DE model: Shear stress and the first and second normal stress differences in the high-shear-rate zone at location $y = 0.05$ (Fig. 8a) and in the low-shear-rate zone at location $y = 0.4$ (Fig. 8b).

6.1.2. Numerical simulation of the flows using the DE, CB, RR and DR models

This section presents the use of the present macro-micro multiscale method to simulate the Couette flow of polymer melt modelled by several other reptation models including the CB, RR and DR to find possible differences by introducing several physical interactions of polymer chains. For instant, the interaction between segments in a single chain by the correlation parameter Δ and the link tension parameter l_1 tis considered for the RR model whereas the DR model focuses on the constraint release mechanism with the parameters l_1, l_2 and l_3.

As presented in Section 4, a polymer melt of the classical reptation models is governed by the system of macro-micro equations (14a)-(14e) with $l_1 = l_2 = l_3 = l_4 = 0$ for the DE model; $l_2 = l_3 = l_4 = 0$ for the CB model; $l_1 = l_2 = l_3 = 0$ for the RR model; and $l_4 = 0$ for the DR model. Hence, the start-up Couette flow of polymer melt is successively simulated using the CB, RR, DR models whose parameters are given and derived from those of the DE model in Section 6.1.1.

The simulating cases together with parameters given in Table 1 where the modulus of rigidity G (G = $Nn_p k_B T$, see the last column) is determined for the DE, CB, RR and DR models, respectively as follows [34]

$$\eta_0^{DE} = \frac{1}{60} Nn_p k_B T \lambda, \tag{42a}$$

$$\eta_0^{CB} = \frac{1}{60}\left(1 + \frac{2}{3}l_1\right) Nn_p k_B T \lambda, \tag{42b}$$

$$\eta_0^{RR} = \frac{1}{60}\left[1 + \frac{2}{3}l_1\Delta^2\left(4 - 6\Delta + 4\Delta^2 - \Delta^3\right)\right] Nn_p k_B T \lambda, \tag{42c}$$

$$\eta_0^{DR} = \frac{1}{60}\left\{\frac{12}{\pi^2 l_2^2}\left[1 - \frac{tanh(\pi l_2/2)}{\pi l_2/2}\right] + \frac{2}{3}l_2 + 4l_3\right\} Nn_p k_B T \lambda. \tag{42d}$$

Table 1. Simulation of the start-up Couette flow of polymer melt using the DE, CB, RR, DR models. Parameters of 16 different cases including six cases of the CB model (CB_{T1} -> CB_{T6}), six cases of the RR model (RR_{T1} -> RR_{T6}) and three cases of the DR model (DR_{T1} -> DR_{T3}) are derived from the DE model as λ = 50, η_o = 1 and l_3 = 0; G = $Nn_p k_B T$: the rigidity modulus of models. Parameters were defined in previous sections.

Cases	Model	l_1	L_2	Δ	G
1	DE	0.00	0	0	1.200
2	CB_{T1}	0.01	0	0	1.192
3	CB_{T2}	0.05	0	0	1.161
4	CB_{T3}	0.10	0	0	1.125
5	CB_{T4}	0.25	0	0	1.029
6	CB_{T5}	0.50	0	0	0.900
7	CB_{T6}	1.00	0	0	0.720
8	RR_{T1}	0.01	0	0	1.200
9	RR_{T2}	0.01	0	0.10	1.200
10	RR_{T3}	0.01	0	0.25	1.199
11	RR_{T4}	0.01	0	0.50	1.196
12	RR_{T5}	0.01	0	0.75	1.194
13	RR_{T6}	0.01	0	1	1.192
14	DR_{T1}	0.00	0.25	0	1.274
15	DR_{T2}	0.00	0.50	0	1.495
16	DR_{T3}	0.00	0.75	0	1.862

Fig. 9 shows the velocity profiles of the Couette flow simulation of CB modelled polymer melts using the present macro-micro multiscale method for a range of values of $l_1 \in [0.01, 1]$ as presented in Table 1 (column 3). The results confirm that the coefficient l_1 reflects the appearance of "two different shear rate regions" which is a distinctive feature of a polymer melt system. Numerical results show that when the value of l_1 increases, the steady velocity of polymer melt system reaches a Newtonian flow (l_1 = 0.5 and 1, Fig. 9). Therefore, an efficiently small value of l_1 (l_1 = 0.01 in this simulation) is necessary to characterise this typical behaviour of polymer melt systems as confirmed by [34].
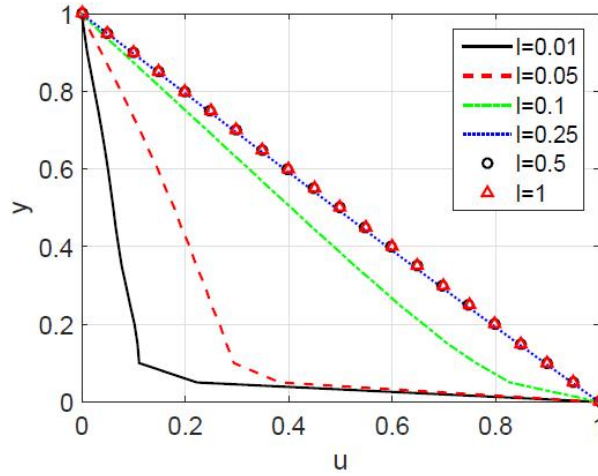
Figure 9. The start-up Couette flow of CB modelled polymer melt using the present multiscale method: The steady velocity profiles of the flow with a range of values of the link tension coefficient l_1 = {0.01, 0.05, 0.1, 0.25, 0.5, 1}. Other parameters of the simulation are given in Section 7.1.1 and in Table 1.

For the RR-modelled polymer melt, the start-up Couette flow is investigated using the present method with the link tension coefficient l_1 of 0.01 and a range of correlation parameter values $\Delta \in$ {0, 0.1, 0.25, 0.5, 0.75, 1} (table 1, column 5). The velocity profile by the simulation for all cases of the flow in Fig. 10 depicts that for the RR modelled polymer melt, the correlation parameter only impacts the shape of the high-shear-rate zone in a shear flow. Indeed, the velocity gradient increases with the increment of Δ.
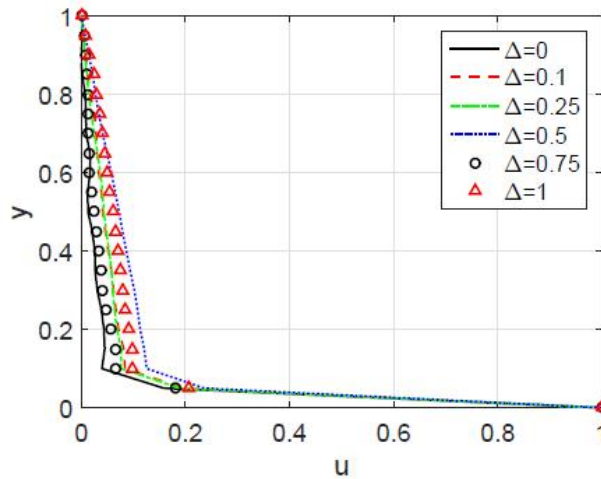
Figure 10. The start-up Couette flow of RR modelled polymer melt: The simulating steady velocity profiles of the flow with a range of values of the correlation length parameter Δ = {0, 0.1, 0.25, 0.5, 0.75, 1} and the link tension coefficient l_1 = 0.01 using the present method. Other parameters of the simulation are given in Section 7.1.1 and in Table 1.

For the DR modelled polymer melt flows governed by Eqs. (14a)-(14e) with l_1 = l_3 = 0, the problem is examined with a range of the parameter $l_2 \in$ {0.25, 0.5, 0.75} (table 1, column 4). The simulating velocity profile by Fig. 11 depicts that the high-shear-rate zone is enlarged with the increment of l_2.
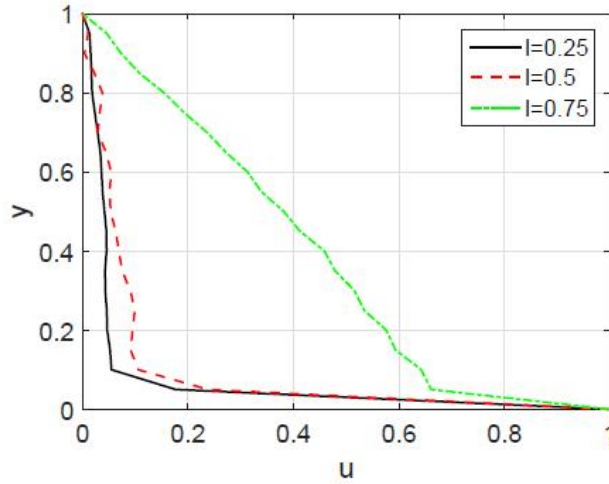
Figure 11. The start-up Couette flow of polymer melt using the DR model: The simulating steady velocity profiles of the flow with l_2 = {0.25, 0.5, 1} and $l_1 = l_3 = 0$ using the present method. Other parameters of the simulation are given in Section 7.1.1 and in Table 1.

Finally, the simulation of the start-up Couette flow of polymer melt modelled by four reptation models: DE, CB_{T1}, RR_{T4} and DR_{T1}, whose parameters are given in table 1, is carried out using the present method in order to possibly highlight typical differences using different models. Numerical results are observed as follows,

- The velocity profiles at the steady state of the flow using the four models presented in Fig.12a show that while there is not any significant change in the low-shear-rate zone, the velocity gradient is stiffer in the order of the RR, CB, DE and DR models in the high-shear-rate zone. Furthermore, the evolution of velocity at location y = 0.5 is also investigated in the high-shear-rate zone (Fig. 12b). Results show that an overshoot is observed in all models at $t \approx 3$ and the velocity then reached nearly the same steady value after different elapsed times as 11, 12, 13 and 18 for the DE, DR, CB and RR models, respectively. In order words, the velocity of the flow needs much more time to reach a steady state for the RR model.

- Last but not least, the evolution of shear stress (τ_{xy}) and the first normal stress difference ψ_1 at location y = 0.5 for the four models are shown in Figs. 13. Results confirm that unlike the velocity field, there is no significant difference of the stresses by the simulation using the four reptation models.
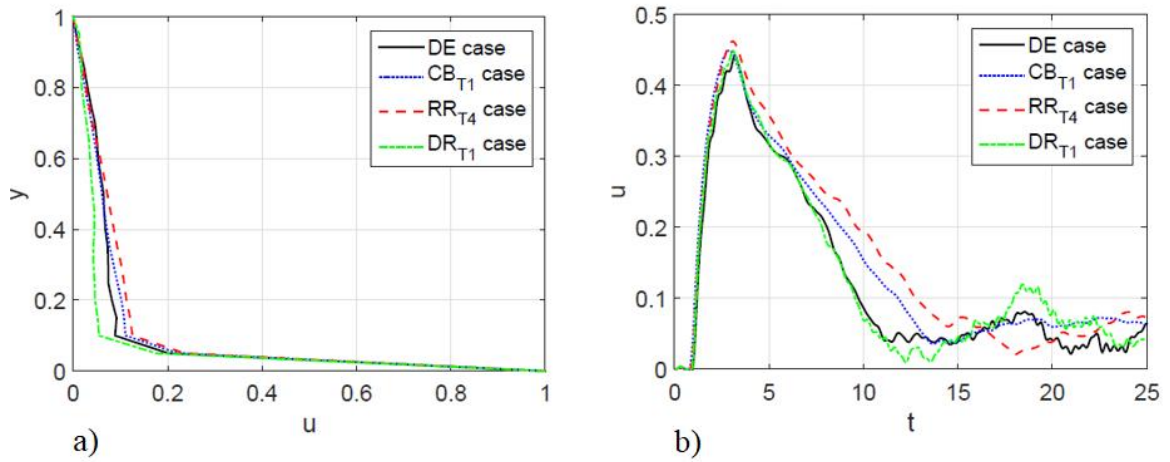
Figure 12. The start-up Couette flow of polymer melt using reptation models DE, CB, RR and DR: a) The steady velocity profiles of the flow; and b) the evolution of the velocity at location $y = 0.5$ using the present method.
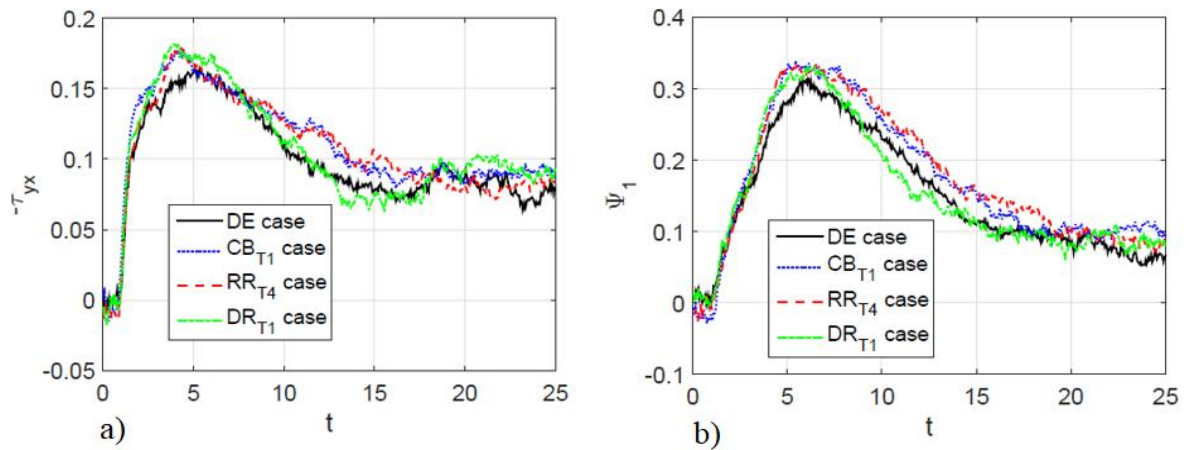
Figure 13. The start-up Couette flow of polymer melt modelled by DE, CB, RR and DR reptation models: a) The evolution of the shear stress (τ_{xy}); and b) the evolution of the first normal stress difference (ψ_1) at the location $y = 0.5$ using the present multiscale method.

6.2. Flow of DE modelled polymer melt past a circular cylinder in a channel

A polymer melt flow past a cylinder in a channel is described in Fig. 14 is simulated using the present method. Owing to the geometrical symmetry, a half of the flow's domain is considered, where $L = 30$ is the total length of the channel; $L_U = 15$ and $L_D = 15$ the upstream and downstream lengths, respectively; $R_c = 1$ the cylinder's radius and $H = 2$ a half of height of the channel. The benchmark problem was studied by [29] using the BCF coupled finite element method (FEM).
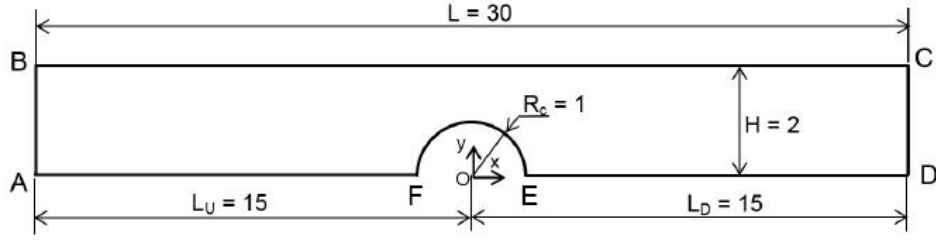
Figure 14. The flow past a circular cylinder in a channel: geometrical parameters of the problem.

6.2.1.   Governing equations and boundary conditions

The stochastic macro-micro governing equations Eq. (12a) - Eq. (12e) of the problem in 2-D Cartesian coordinate are developed as follows.

$$\frac{\partial u}{\partial x} + \frac{\partial v}{\partial y} = 0 \tag{43}$$

$$\begin{cases} D_P\left[\left(\frac{\partial^2 u}{\partial x^2} + \frac{\partial^2 u}{\partial y^2}\right) - \left(\frac{\partial^2 u_0}{\partial x^2} + \frac{\partial^2 u_0}{\partial y^2}\right)\right] - \frac{\partial p}{\partial x} + \frac{\partial \tau_{p,xx}}{\partial x} + \frac{\partial \tau_{p,xy}}{\partial y} = 0 \\[4mm] D_P\left[\left(\frac{\partial^2 v}{\partial x^2} + \frac{\partial^2 v}{\partial y^2}\right) - \left(\frac{\partial^2 v_0}{\partial x^2} + \frac{\partial^2 v_0}{\partial y^2}\right)\right] - \frac{\partial p}{\partial y} + \frac{\partial \tau_{p,xy}}{\partial x} + \frac{\partial \tau_{p,yy}}{\partial y} = 0 \end{cases} \tag{44}$$

$$dS(t) = \sqrt{\frac{2}{\pi^2 We}} dW_1(t), \tag{45}$$

$$\begin{cases} dP_x = \frac{\partial u}{\partial y}(y,t) P_y(y,t) dt + \frac{l_2}{\sqrt{3We}} dW_{2x} - \frac{l_2^2}{3We} P_x(y,t) dt, \\[4mm] dP_y = \frac{l_2}{\sqrt{3We}} dW_{2y} - \frac{l_2^2}{3We} P_y(y,t) dt, \\[4mm] dP_z = \frac{l_2}{\sqrt{3We}} dW_{2z} - \frac{l_2^2}{3We} P_z(y,t) dt, \end{cases} \tag{46}$$

$$\begin{cases} \tau_{p,xx} = Nn_p k_B T\left[\frac{1}{3} - \langle P_x P_x \rangle\right], \ \tau_{p,yy} = Nn_p k_B T\left[\frac{1}{3} - \langle P_y P_y \rangle\right], \\[4mm] \tau_{p,zz} = Nn_p k_B T\left[\frac{1}{3} - \langle P_z P_z \rangle\right], \ \tau_{p,xy} = -Nn_p k_B T\langle P_x P_y \rangle, \end{cases} \tag{47}$$

where parameters and variables are defined in previous sections. The boundary conditions are determined correspondingly to ones by [29] as

- At the inlet $\overline{AB}$, the fully developed velocity profile u is set up. The velocity profile is pre-determined by simulating the corresponding Poiseuille flow through a long channel using the same polymer melt model with a parabolic velocity profile $u = 1.5\left(1 - y^2/H^2\right)$ and v = 0 where u and v are the velocity components along the *x* and *y* directions, respectively, and other parameters are defined as before. Meanwhile the boundary condition for pressure is calculated at each time step as presented in section 5.1.2.

- At the outlet $\overline{CD}$, the fully developed velocity profile u is also set up as presented for the inlet, v = 0 and pressure *p* = 0.

- On the channel wall $\overline{BC}$ and the cylinder wall $\overline{FE}$, the non-slip boundary conditions for the velocity: u = v = 0 are set up whereas the boundary condition of pressure is calculated at each time step as presented in section 5.1.2.

- On the centreline $\overline{AF}$ and $\overline{ED}$, the symmetrical boundary condition of the velocity field is applied as $\partial u/\partial y = 0$ and v = 0 and the Neumann boundary condition for pressure is determined at each time step as mentioned in section 5.1.2.

A pseudo time method combined with the projection technique presented in section 5.1 is used to temporally discretise Eqs. (44) whereas the explicit time discretisation method is applied to Eqs. (46). These discretisations of Eqs. (44) and Eqs. (46) yield, respectively

$$
\begin{cases}
u^{n+1} - D_P \Delta t \left(\dfrac{\partial^2 u^{n+1}}{\partial x^2} + \dfrac{\partial^2 u^{n+1}}{\partial y^2} \right) + \Delta t \dfrac{\partial p^{n+1}}{\partial x} = u^n - D_P \Delta t \left(\dfrac{\partial^2 u^n}{\partial x^2} + \dfrac{\partial^2 u^n}{\partial y^2} \right) \\
\qquad\qquad\qquad\qquad\qquad\qquad\qquad\qquad + \Delta t \left(\dfrac{\partial \tau_{p,xx}}{\partial x} + \dfrac{\partial \tau_{p,xy}}{\partial y} \right), \\[4pt]
v^{n+1} - D_P \Delta t \left(\dfrac{\partial^2 v^{n+1}}{\partial x^2} + \dfrac{\partial^2 v^{n+1}}{\partial y^2} \right) + \Delta t \dfrac{\partial p^{n+1}}{\partial y} = v^n - D_P \Delta t \left(\dfrac{\partial^2 v^n}{\partial x^2} + \dfrac{\partial^2 v^n}{\partial y^2} \right) \\
\qquad\qquad\qquad\qquad\qquad\qquad\qquad\qquad + \Delta t \left(\dfrac{\partial \tau_{p,xy}}{\partial x} + \dfrac{\partial \tau_{p,yy}}{\partial y} \right),
\end{cases}
\tag{48}
$$

$$
\begin{cases}
P_x^{n+1} = P_x^n + \left(\dfrac{\partial u^{n+1}}{\partial x} P_x^n + \dfrac{\partial u^{n+1}}{\partial y} P_y^n \right) \Delta t - \left(u^{n+1} \dfrac{\partial P_x^n}{\partial x} + v^{n+1} \dfrac{\partial P_x^n}{\partial y} \right) \Delta t \\[4pt]
P_y^{n+1} = P_y^n + \left(\dfrac{\partial v^{n+1}}{\partial x} P_x^n + \dfrac{\partial v^{n+1}}{\partial y} P_y^n \right) \Delta t - \left(u^{n+1} \dfrac{\partial P_y^n}{\partial x} + v^{n+1} \dfrac{\partial P_y^n}{\partial y} \right) \Delta t \\[4pt]
P_z^{n+1} = P_z^n - \left(u^{n+1} \dfrac{\partial P_z^n}{\partial x} + v^{n+1} \dfrac{\partial P_z^n}{\partial y} \right) \Delta t
\end{cases}
\tag{49}
$$

The velocity and velocity gradient in the micro process governed by Eqs. (49) are known and given by the solution of Eqs. (48) of the macro process.

For the present method, the time step size is chosen Δt = 0.001 as used in [29]. The parameters of fluid include N_f = 2000, λ = 1, We =λ/π^2, $\eta_0^{DE} = 1$ and the rigidity modulus G and damping parameter D_P for the DE model which are determined, respectively as follows.

$$G = Nn_p k_B T = \frac{60\eta_0^{DE}}{\lambda} = 60, \qquad D_P = \frac{G\Delta t}{\eta_0^{DE}} = 0.06, \tag{50}$$

where the parameters are defined as before.

6.2.2. Numerical results and discussion

Firstly, a grid convergence study is performed using 3 non-uniform Cartesian grids of collocation points whose parameters are detailed in Table 2 and Fig. 15. The three grids are labelled as M1, M2 and M3 where M1 is the coarsest and M3 is the finest.

Table 2. The flow past a circular cylinder in a channel. The parameters of the three grids of collocation points M1, M2 and M3. Δx_1: the grid spacing in x-direction $\forall x \in [-15,-5] \cup [5,15]$, Δx_2 $\forall x \in [-5,-2] \cup [2,5]$, Δx_3 $\forall x \in [-2,-1] \cup [1,2]$; Δy: the grid spacing in y-direction $\forall y \in [0,2] \cup [5,15]$, N_{cyn}: the number of collocation points on the cylinder's surface and N: the number of collocation points on the whole domain.

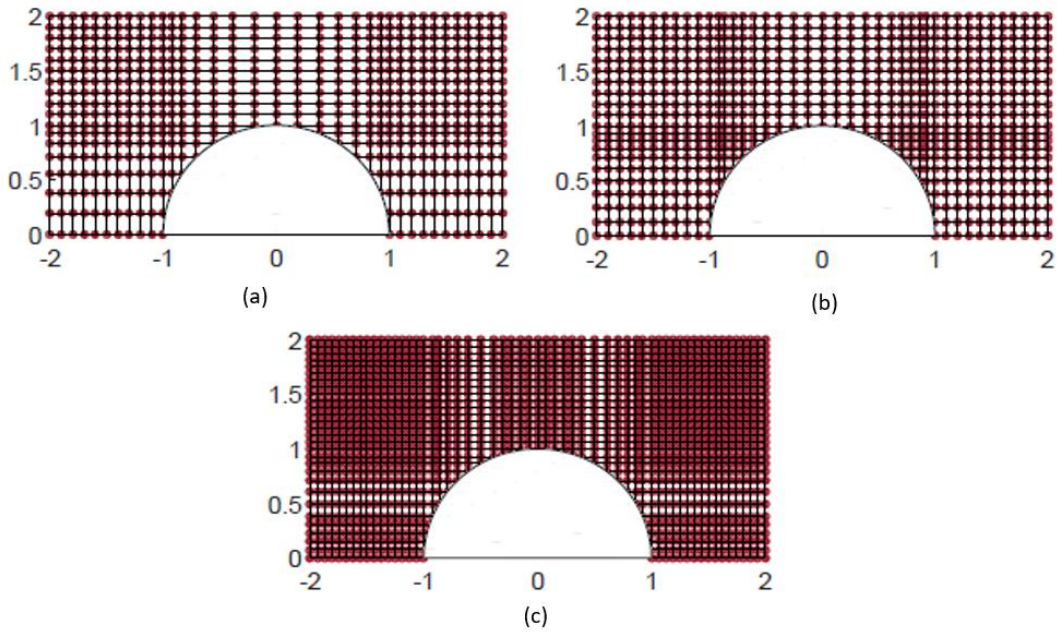| Grid	Δx_1	Δx_1	Δx_1	Δx_1	N_{cyn}	N
M1	0.5	0.3	0.1	0.1	17	1649
M2	0.5	0.3	0.1	0.1	25	1991
M3	0.4	0.2	0.0625	0.0625	33	3761

Figure 15. The schematic non-uniform Cartesian grids of collocation points at the region around the cylinder for 3 cases M1 (a), M2 (b) and M3 (b) as detailed in table 2.

The numerical experiment by the present method shows that the convergence of the velocity field reached in the simulation of the problem using the 3 grids M1, M2 and M3 (see Fig. 16).
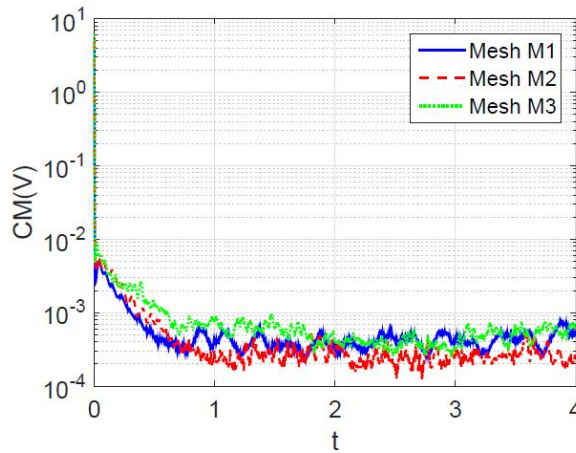

Figure 16. The flow past a circular cylinder in a channel: The convergence measure of the velocity field with grid refinement.

The results by the present method confirm a very good agreement with those by [29] using FEM with the same time step (Δt = 0.001). Details are presented as follows.

- The velocity profile in the gap between the wall and the cylinder is shown in Fig. 17. The numerical result of Newtonian fluid included in the figure shows the difference between polymer melt and Newtonian flows. A symmetrical parabolic shape is for the Newtonian profile whereas an asymmetrical bell-shaped profile is observed in the simulation of polymer melt flow. That can

be explained as the velocity gradient at the region near the cylinder wall is steeper than one near the channel wall for the polymer melt flows as observed in Fig. 18 whereas it is linear for the Newtonian fluid.

Results by Fig. 17 also show that the maximum values of the velocity profiles at the middle point of the gap are approximate 2.9 and 2.7 for the Newtonian and the polymer melt flows using mesh M3, respectively. The obtained results are in excellent agreement with those stated in Figs. 6 and 7 by [29].

Furthermore, the distribution of velocity field by contours in the considered domain depict a smooth change of the velocity components u, v around the cylinder in Figs. 19a and 19b, respectively and the velocity field describing the flow movement around the cylinder in Fig. 19c.
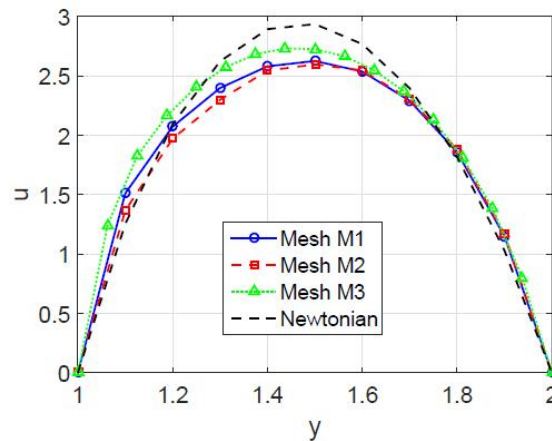
Figure 17. The flow past a cylinder in a channel: The velocity profile in the gap between the wall and the cylinder for polymer melts with the 3 grids (M1, M2 and M3) of collocations and for Newtonian fluid using M3.
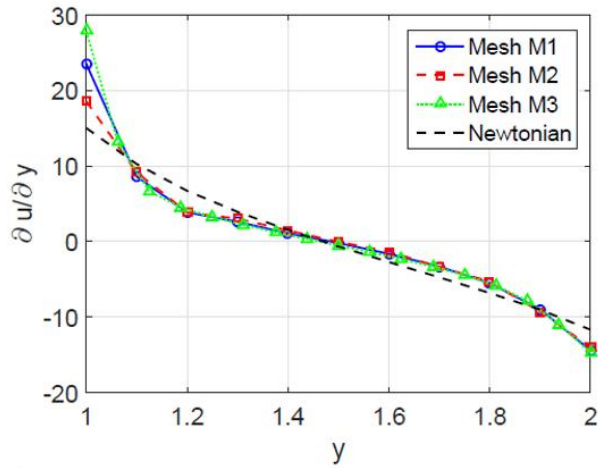
Figure 18. The flow past a cylinder in a channel: The velocity gradient $\partial u / \partial y$ in the gap between the wall and the cylinder for polymer melts with the 3 grids of collocations (M1, M2 and M3) and for Newtonian fluid using grid of collocations M3.
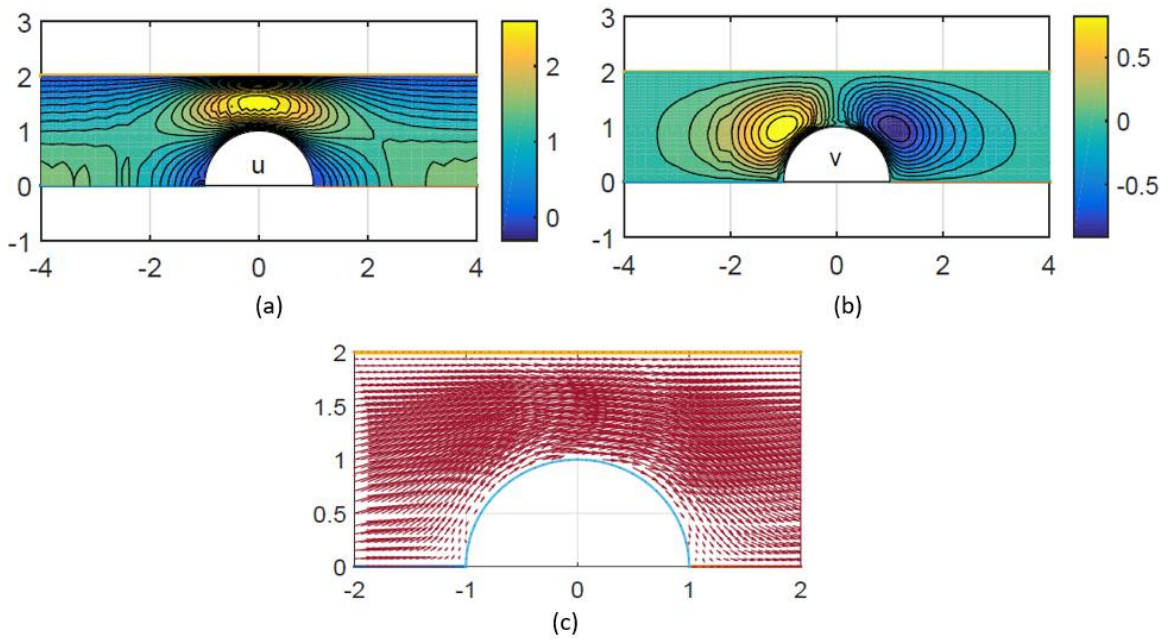

Figure 19. The flow past a cylinder in a channel using Mesh M3: (a) the contour value of velocity component u; (b) the contour value of velocity component v; and (c) the distribution of the velocity around the cylinder.
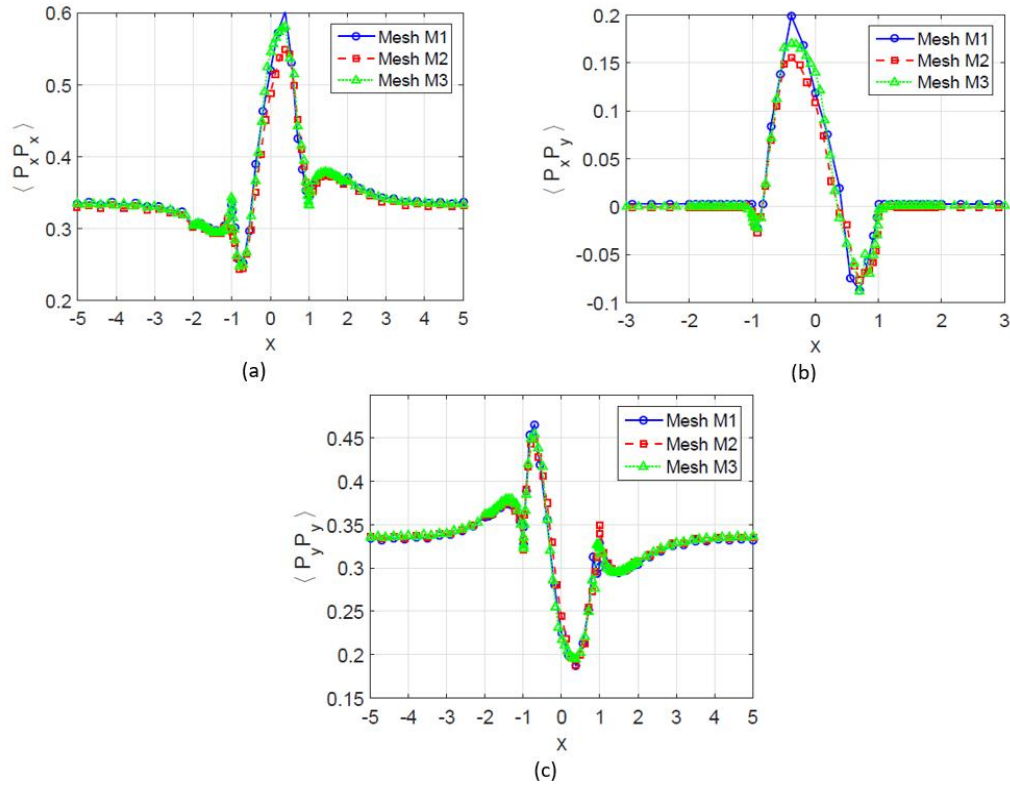
Figure 20. The flow past a cylinder in a channel: (a) the distribution of $\langle P_x P_x \rangle$; (b) the distribution of $\langle P_x P_y \rangle$; and (c) the distribution of $\langle P_y P_y \rangle$ of the orientation tensor $\langle \mathbf{PP} \rangle$ along the centreline y = 0 and the cylinder's surface.

- Since the distribution of stresses of polymer melt flows in the considered domain are determined based on the orientation tensor $\langle \mathbf{PP} \rangle$ as shown by Eqs. (47), the distribution of the components of $\langle \mathbf{PP} \rangle$ along the centreline and the cylinder's surface is studied and presented in Figs. 20(a), 20(b) and 20(c) for $\langle P_x P_x \rangle$, $\langle P_x P_y \rangle$, $\langle P_y P_y \rangle$, respectively with the three different grids of collocation points on the range of $x \in [-1,1]$. The simulating results by the present method confirmed a very good agreement with those presented in [29] using the BCF-finite element method with a finer mesh. In addition, the contours with 20 levels of the $\langle P_x P_x \rangle$, $\langle P_x P_y \rangle$, $\langle P_y P_y \rangle$ components around the cylinder by the present method are also presented in Figs. 21(a), (b) and (c), respectively. One of them, the $\langle P_x P_x \rangle$ -contours studied by a benchmark paper of [29] (Fig. 8) are in very good agreement with results described in Fig. 21(a) of this work.
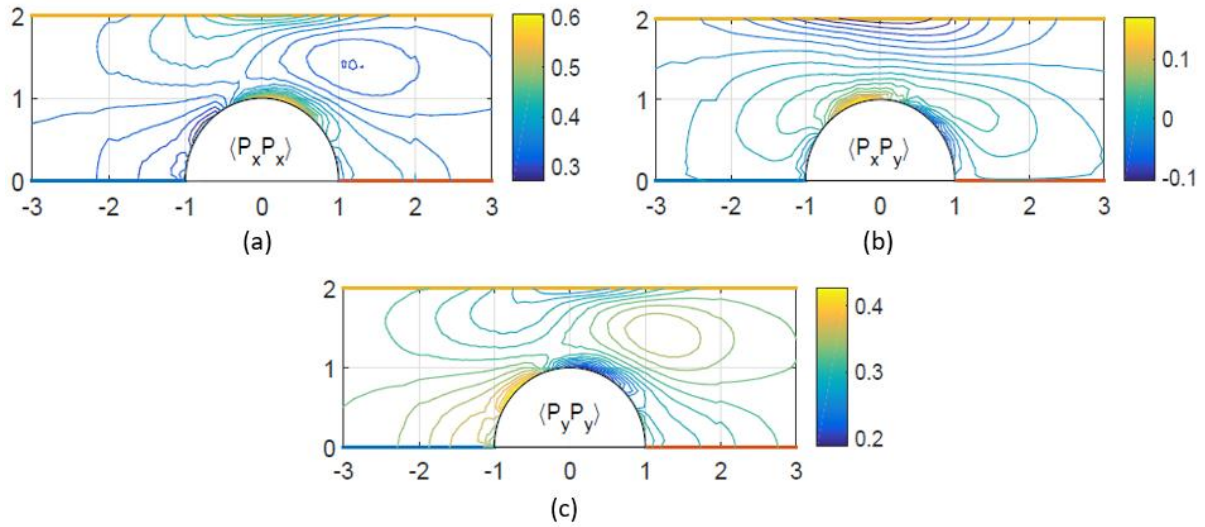
Figure 21. The flow past a cylinder in a channel using Mesh M3: The contour levels of the xx (a), xy (b) and yy (c) components of the tensor $\langle \mathbf{PP} \rangle$ around the cylinder.

- The pressure distribution on the cylinder's surface is also studied and simulated using our present multiscale method with three meshes M1, M2 and M3. The results by Fig. 22 show that the pressure gradually increases from the starting point E ($\theta = 0$) to the end point F ($\theta = \pi$) of the cylinder (see Fig. 14) where θ is the angle defining the position of the collocation point on the cylinder's surface. Also, the pressure distribution on the cylinder's surface corresponding to the Newtonian fluid is simulated and included in the figure for the comparison. Results by Fig. 22 show that the pressure gradient of the Newtonian fluid is steeper than one of the polymer melts. Indeed, starting from nearly the same pressure (p ~ 9) within $\theta \in [0, \pi / 4]$, the pressure of the Newtonian flow increases to reach a maximum value of $p = 59$ versus $p = 49$ for the polymer melts at $\theta = \pi$.
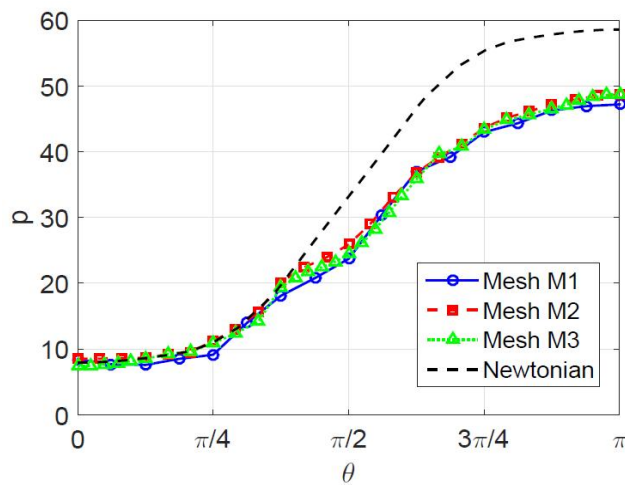
Figure 22. The flow past a cylinder in a channel: The distribution of pressure on the cylinder's surface for polymer melts with the 3 grids of collocations (M1, M2 and M3) and for Newtonian fluid using grid of collocations M3.

- It is worth noting that together with pressure, it is necessary to determine the drag force per unit length while polymer melt moves over a cylinder in a channel. The force of the fluid exerts on the cylinder is given by [43]

$$F_D = -2\int_0^\pi \left[\left(-p + \tau_{p,xx} \right) \cos\theta + \tau_{p,xy} \sin\theta \right]_{r=R} R d\theta \ . \tag{51}$$

The dimensionless drag force per a unit length K is calculated as $K = F_D / \eta_0^{DE} U_c$, where U_c is the characteristic velocity and other parameters were defined before. U_c and η_0^{DE} are chosen as 1 in this work.

The evolution of the dimensionless drag force K using three grids of collocation points M1, M2 and M3 by Fig. 23 shows the drag force K increases quickly and reaches stable value at 93 for the polymer melt flow. The results by the present method are in very good agreement with one by van Heel et al. [29], except a small fluctuation observed for the use of the coarse grid M1.
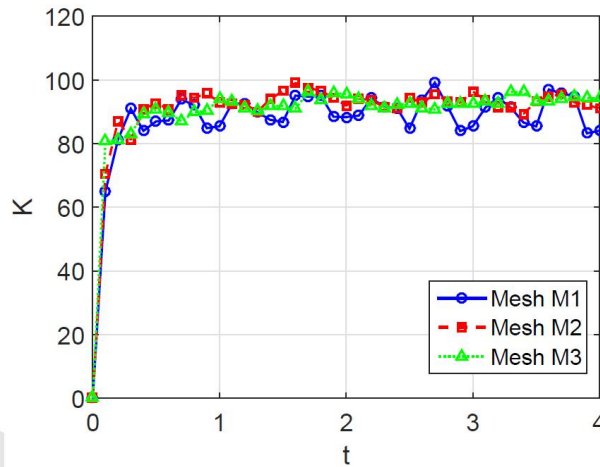

Figure 23. The flow past a cylinder in a channel: The evolution of the drag force per unit length exerted on the cylinder for polymer melts using three grids of collocation points M1, M2 and M3.

Finally, it is worth noting that the present Integrated RBF based stochastic multiscale simulation method enhances the computation time compared with the previous stochastic simulation ones (for example, the CONNFFESSIT approach [37]) by possibly using coarse grids of collocation points and/or a bigger time step size (0.001 instead of 0.0001, see section 6.1) owing to the high order RBF approximation functions.

7. Conclusions

The IRBF-BCF based stochastic multiscale method is further developed and investigated to simulate polymer melt flows using different reptation models in this paper. For our present method, the macro procedure governed by conservation equations is solved for the primitive variables including the velocity and pressure using 1D-IRBFN scheme, whereas the IRBF coupled BCF coarse-grained approach is used to determine polymer stress matrix from the obtained stochastic processes associated with a reptation model. The numerical results by the simulation of the start-up planar Couette flow and specially the benchmark flow past a cylinder in a channel of polymer melts modelled by different reptation models, for example, the DE, CB, RR and DR models presented in Section 6 confirm the method efficiency on both the enhanced convergence rate of the solution and the stability of a stochastic process.

References

[1]   R. B. Bird, C. F. Curtiss, R. C. Armstrong, and O. Hassager, *Dynamics of polimeric liquids, Vol 2: Kinetic theory*, The first. New York: John Wiley & Sons, 1987.

[2]   P. G. de Gennes, "Reptation of a polymer chain in the presence of fixed obstacles," *J Chem Phys*, vol. 55, pp. 572–579, 1971. https: Doi:10.1063/1.1675789

[3]   M. Doi and S. F. Edwards, "Dynamics Of Concentrated Polymer Systems. Part 1: Brownian motion in the equilibrium state," *J. Chem. Soc., Faraday Trans. II*, vol. 74, pp. 1789–1801, 1978, Doi: 10.1039/F29787401789.

[4]   M. Doi and S. F. Edwards, "Dynamics Of Concentrated Polymer Systems. Part 2: Molecular-Motion Under Flow," *J. Chem. Soc., Faraday Trans. II*, vol. 74, pp. 1802–1817, 1978, Doi: 10.1039/F29787401802.

[5]   M. Doi and S. F. Edwards, "Dynamics Of Concentrated Polymer Systems. Part 3: Constitutive Equation," *J. Chem. Soc., Faraday Trans. II*, vol. 74, pp. 1818–1832, 1978, Doi: 10.1039/F29787401818.

[6]   C. F. Curtiss and R. B. Bird, "A kinetic theory for polymer melts. I. The equation for the single-link orientational distribution function," *J Chem Phys*, vol. 74, pp. 2016–2025, 1981. Doi: 10.1063/1.441246

[7]   C. F. Curtiss and R. B. Bird, "A kinetic theory for polymer melts. II. The stress tensor and the rheological equation of state," *J Chem Phys*, vol. 74, pp. 2026–2033, 1981. Doi: 10.1063/1.441247

[8]   R. B. Bird, H. H. Saab, and C. F. Curtiss, "A kinetic theory for polymer melts. III. Elongational flows," *J Phys Chem*, vol. 86, no. 7, pp. 1102–1106, 1982. Doi: 10.1021/j100396a011

[9]   R. B. Bird, H. H. Saab, and C. F. Curtiss, "A kinetic theory for polymer melts. IV. Rheological properties for shear flows," *J Chem Phys*, vol. 77, pp. 4747–4757, 1982. Doi: 10.1063/1.444378

[10]   R. J. J. Jongschaap, "Some Comments on Reptation Theories," in *Progress and Trends in Rheology II. Proceedings of the Second Conference of European Rheologists, Prague, June 17–20, 1986*, H. Giesekus and M. F. Hibberd, Eds. Prague: Springer, 1988, pp. 99–102.

[11]   R. J. J. Jongschaap and B. J. Geurts, "A New Reptation Model for Polymeric Liquids," in *Integration of Fundamental Polymer Science and Technology - 2*, P. J. Lemstra and L. A. Kleintjens, Eds. 1988, pp. 461–465. Doi: 10.1007/978-94-009-1361-5_69

[12]   J. des Cloizeaux, "Double Reptation vs. Simple Reptation in Polymer Melts," *Europhys Lett*, vol. 5, pp. 437–442, 1988. Doi: 10.1209/0295-5075/5/5/010

[13]   H. C. Ottinger, "Computer simulation of reptation theories. I. Doi-Edwards and Curtiss-Bird models," *J Chem Phys*, vol. 91, pp. 6455–6462, 1989. Doi: 10.1063/1.457361

[14]   H. C. Ottinger, "Computer simulation of reptation theories. II. Reptating rope model," *J Chem Phys*, vol. 92, pp. 4540–4547, 1990. Doi: 10.1063/1.457714

[15]   H. C. Ottinger and M. Laso, "Smart polymers in finite element calculation," *Theoretical and Applied Rheology*, vol. 1, pp. 286–288, 1992.

[16]   R. Keunings, "Micro-macro methods for the multiscale simulation of viscoelastic flow using molecular models of kinetic theory. Rheology Reviews," *Rheology Reviews*, pp. 67–98, 2004.

[17]   M. A. Hulsen, A. P. G. van Heel, and B. H. A. A. van den Brule, "Simulation of viscoelastic flows using Brownian configuration fields," *J Nonnewton Fluid Mech*, vol. 70, no. 1, pp. 79–101, 1997. Doi: 10.1016/S0377-0257(96)01503-0

[18]   D. Tran-Canh and T. Tran-Cong, "Computation of viscoelastic flow using neural networks and stochastic simulation," *Korea-Australia Rheology Journal*, vol. 14, no. 2, pp. 161–174, 2002.

[19]   D. Tran-Canh and T. Tran-Cong, "Element-free simulation of dilute polymeric flows using Brownian Configuration Fields," *Korea-Australia Rheology Journal*, vol. 16, no. 1, pp. 1–15, 2004.

[20]   C.-D. Tran, D. G. Phillips, and T. Tran-Cong, "Computation of dilute polymer solution flows using BCF-RBFN based method and domain decomposition technique," *Korea-Australia Rheology Journal*, vol. 21, no. 1, pp. 1–12, 2009.

[21]   N. Mai-Duy, K. Le-Cao, and T. Tran-Cong, "A Cartesian grid technique based on one-dimensional integrated radial basis function networks for natural convection in concentric annuli," *Int J Numer Methods Fluids*, vol. 57, no. 12, 2008. Doi: 10.1002/fld.1675

[22]   C. M. T. Tien, N. Thai-Quang, N. Mai-Duy, C.-D. Tran, and T. Tran-Cong, "A three-point coupled compact integrated RBF scheme for second-order differential problems," *CMES - Computer Modeling in Engineering and Sciences*, vol. 104, no. 6, pp. 425–469, 2015.

[23]   C.-D. Tran, N. Mai-Duy, K. Le-Cao, and T. Tran-Cong, "A continuum-microscopic method based on IRBFs and control volume scheme for viscoelastic fluid flows," *CMES - Computer Modeling in Engineering and Sciences*, vol. 85, no. 6, pp. 499–519, 2012.

[24]   C.-D. Tran, D.-A. An-Vo, N. Mai-Duy, and T. Tran-Cong, "An integrated RBFN-based macro-micro multi-scale method for computation of visco-elastic fluid flows," *CMES - Computer Modeling in Engineering and Sciences*, vol. 82, no. 2, pp. 137–162, 2011.

[25]   H. Q. Nguyen, C.-D. Tran, and T. Tran-Cong, "A multiscale method based on the fibre configuration field, IRBF and DAVSS for the simulation of fibre suspension flows," *CMES - Computer Modeling in Engineering and Sciences*, vol. 109, no. 4, pp. 361–403, 2015.

[26]   H. Nguyen and C.D. Tran, "Simulation of non-dilute fibre suspensions using RBF-based macro–micro multiscale method," *Korea-Australia Rheology Journal*, vol. 34, no. 1, pp. 1–15, 2022. Doi: 10.1007/s13367-022-00022-1

[27]   H. Q. Nguyen, C.-D. Tran, and T. Tran-Cong, "RBFN stochastic coarse-grained simulation method: Part I - Dilute polymer solutions using bead-spring chain models," *CMES - Computer Modeling in Engineering and Sciences*, vol. 105, no. 5, pp. 399–439, 2015.

[28]   C. C. Hua and J. D. Schieber, "Viscoelastic flow through fibrous media using the CONNFFESSIT approach," *J Rheology*, vol. 42, pp. 477–491, 1998. Doi: 10.1122/1.550960

[29]   A. P. G. van Heel, M. A. Hulsen, and B. H. A. A. van den Brule, "Simulation of the Doi-Edwards model in complex flow," *J Rheology*, vol. 43, pp. 1239–1260, 1999. Doi: 10.1122/1.551022

[30]   B. Bernstein, E. Kearsley, and L. Zapas, "A study of stress relaxation with finite strain," *Transactions of The Society of Rheology*, vol. 7, no. 1, pp. 391–410, 1963. Doi:10.1122/1.548963

[31]   A. Kaye, *Non-Newtonian flow in incompressible fluids*. College of Aeronautics Cranfield, 1962.

[32]   N. Phan-Thien and R. I. Tanner, "A new constitutive equation derived from network theory," *J Nonnewton Fluid Mech*, vol. 2, no. 4, pp. 353–365, 1977. Doi: 10.1016/0377-0257(77)80021-9

[33]   T. C. B. McLeish and R. G. Larson, "Molecular constitutive equations for a class of branched polymers: The pom-pom polymer," *J Rheology*, vol. 42, no. 1, pp. 81–110, 1998. Doi: 10.1122/1.550933

[34]   H. C. Ottinger, *Stochastic processes in polymeric fluids: tools and examples for developing simulation algorithms*. Berlin: Springer, 1996.

[35]   Y. Masubuchi, "Simulating the flow of entangled polymers," *Annu Rev Chem Biomol Eng*, vol. 5, pp. 11–33, 2014. Doi:10.1146/annurev-chembioeng-060713-040401

[36]   N. Thai-Quang, N. Mai-Duy, C.-D. Tran, and T. Tran-Cong, "High-order alternating direction implicit method based on compact integrated-rbf approximations for unsteady/steady convection-diffusion equations," *CMES - Computer Modeling in Engineering and Sciences*, vol. 89, no. 3, 2012.

[37]   H. C. Ottinger and M. Laso, "Bridging the gap between molecular models and viscoelastic flow calculations," in *Technical Papers of the Annual Technical Conference*, Society of Plastics Engineers Incorporated, 1995, pp. 2604–2618. Doi: 10.1371/journal.pone.0014070

[38]   C. C. Hua and J. D. Schieber, "Application of kinetic theory models in spatiotemporal flows for polymer solutions, liquid crystals and polymer melts using the CONNFFESSIT approach," *Chem Eng Sci*, vol. 51, pp. 1473–1485, 1996. Doi: 10.1016/0009-2509(95)00304-5

[39]   D. S. Malkus, J. A. Nohel, and B. J. Plohr, "Dynamics of shear flow of a non-Newtonian fluid," *J Comput Phys*, vol. 87, no. 2, pp. 464–487, 1990. Doi: 10.1016/0021-9991(90)90261-X

[40]   T. C. B. McLeish and R. C. Ball, "A molecular approach to the spurt effect in polymer melt flow," *J Polym Sci B Polym Phys*, vol. 24, no. 8, pp. 1735–1745, 1986. Doi: 10.1002/polb.1986.090240809

[41]   A. N. Beris, M. Avgousti, and A. Souvaliotis, "Spectral calculations of viscoelastic flows: evaluation of the Giesekus constitutive equation in model flow problems," *J Nonnewton Fluid Mech*, vol. 44, pp. 197–228, 1992. Doi: 10.1016/0377-0257(92)80051-X

[42]   M. Keentok, A. G. Georgescu, A. A. Sherwood, and R. I. Tanner, "The measurement of the second normal stress difference for some polymer solutions," *J Nonnewton Fluid Mech*, vol. 6, no. 3–4, pp. 303–324, 1980. Doi: 10.1016/0377-0257(80)80008-5

[43]   N. Phan-Thien and H.-S. Dou, "Viscoelastic flow past a cylinder: drag coefficient," *Comput Methods Appl Mech Eng*, vol. 180, no. 3, pp. 243–266, 1999. Doi: 10.1016/S0045-7825(99)00168-1